Inter-comparison of multiple two-way coupled meteorology and air quality models (WRF v4.1.1-CMAQ v5.3.1, WRF-Chem v4.1.1, and WRF v3.7.1-CHIMERE v2020r1) in eastern China

Chao Gao[1, 2], Xuelei Zhang[1, 2, *]Aijun Xiu[1, 2, *], Qingqing Tong[1, 2], Hongmei Zhao[1, 2], Shichun Zhang[1, 2], Guangyi Yang[1, 2, 3], Mengduo Zhang[1, 2, 3], and Shengjin Xie[1, 2, 4]

[1]Key Laboratory of Wetland Ecology and Environment, State Key Laboratory of Black Soils Conservation and Utilization, Northeast Institute of Geography and Agroecology, Chinese Academy of Sciences, Changchun, 130102, China

[2]Key Laboratory of Wetland Ecology and Environment, Northeast Institute of Geography and Agroecology, Chinese Academy of Sciences, Changchun, 130102, China

[3]University of Chinese Academy of Sciences, Beijing, 100049, China

[4]School of Environment, Harbin Institute of Technology, 150000, Harbin, China

Correspondence to: X.L. Zhang (zhangxuelei@iga.ac.cn) & A.J. Xiu (xiuaijun@iga.ac.cn)

Abstract

Two-way coupled meteorology and air quality models, which account for aerosol–radiation–cloud interactions, have been employed to simulate meteorology and air quality more realistically. Although numerous related studies have been conducted, none compared the performances of multiple two-way coupled models in simulating meteorology and air quality over eastern China. Thus, we systematically evaluated annual and seasonal meteorological and air quality variables simulated by three open-sourced, widely utilized two-way coupled models (Weather Research and Forecasting (WRF)–Community Multiscale Air Quality (WRF–CMAQ), WRF coupled with chemistry (WRF–Chem), and WRF coupled with a regional chemistry-transport model named CHIMERE (WRF–CHIMERE)) by validating their results with surface and satellite observations for eastern China in 2017. Although we have made every effort to evaluate these three coupled models under configurations as consistent as possible, there are still unavoidable differences in the treatments of physical and chemical processes in them. Our thorough evaluations revealed that all three two-way coupled models reasonably captured the annual and seasonal spatiotemporal characteristics of meteorology and air quality. Notably, the roles of aerosol–cloud interaction (ACI) in improving the models' performances were limited compared to those of aerosol–radiation interaction (ARI). The sources of uncertainties and bias among the different ACI schemes in the two-way coupled models were identified. With sufficient computational resources, these models can provide more accurate air quality forecasting to support atmospheric environment management and deliver timely warning of heavy air pollution events. Finally, we proposed potential improvements of two-way coupled models for future research.

1 Introduction

Aerosols in the atmosphere due to anthropogenic and nature emissions not only cause air pollution but also induce climate and meteorological impacts through aerosol-radiation interaction and aerosol-cloud interaction (Carslaw et al., 2010; Rosenfeld et al., 2014; Fan et al., 2016; IPCC, 2021). The feedbacks of aerosols to meteorology have been widely investigated by two-way coupled meteorology and air quality models in the past two decades (Jacobson, 1994, 1997, 1998, 2001, 2002; Grell et al., 2005; Wong et al., 2012; Wang et al., 2014; Zhou et al., 2016; Briant et al., 2017; Feng et al., 2021). In these models, two-way interactions between meteorology and aerosols are enabled by including all the processes involving ARI or/and ACI (Grell and Baklanov, 2011; Wang et al., 2014; Briant et al., 2017; Wang et al., 2021). The fundamental theories, modeling technics, developments, and applications of two-way coupled meteorology and air quality models in North America, Europe and Asia have been systemically reviewed (Zhang, 2008; Baklanov et al., 2014; Gao et al., 2022).

As pointed out by these review papers, the treatments and parameterization schemes of all the physiochemical processes involving ARI and ACI can be very different in two-way coupled models, so that the simulation results from these models could vary in many aspects. At the same time, the configurations of coupled models, such as meteorological and chemical initial and boundary conditions (ICs and BCs), horizontal and vertical resolutions, and emission inventories and processing tools, etc., play important roles in models' simulations. In the past, model inter-comparison projects have been carried out targeting various two-way coupled meteorology and air quality models. For example, the Air Quality Model Evaluation International Initiative Phase II focused on the performance of multiple two-way coupled models and the effects of aerosol feedbacks in Europe and the United States (Brunner et al., 2015; Im et al., 2015a, b; Makar et al., 2015a, b). In Asia, the Model Inter-Comparison Study for Asia Phase III was conducted to evaluate ozone (O_3) and other gaseous pollutants, fine particular matter ($PM_{2.5}$), and acid and reactive nitrogen deposition with various models with/out ARI or/and ACI (Li et al., 2019; Chen et al., 2019; Itahashi et al., 2020; Ge et al. al., 2020; Kong et al., 2020). With respect to this project, Gao et al. (2018, 2020) have reviewed in detail the model performance of seven two-way coupled models from different research groups in simulating a heavy air pollution episode during January 2010 in North China Plain and how aerosol feedbacks affected simulations of meteorological variables and $PM_{2.5}$ concentrations. Targeting the heavy polluted India region, Govardhan et al. (2016) compared aerosol optical depth (AOD) and various aerosol species (black carbon, mineral dust, and sea salt) modeled by WRF-Chem (with ARI) and Spectral Radiation-Transport Model for Aerosol Species (with both ARI and ACI), but under different model configurations.

So far, there is no comprehensive comparisons of multiple coupled models under the same model configuration with respect to the high aerosol loading region over eastern China, where has experienced rapid growth of economy, urbanization, population, as well as severe air quality problems in the past decades (He et al., 2002; Wang and Hao, 2012; Gao et al., 2017; Geng et al., 2021). In the eastern China region (ECR), several open-source and proprietary two-way coupled models have been applied to investigate the ARI and/or ACI effects, yet most studies have focused on certain short-term episodes of heavy air pollution without any year-long simulations (Xing et al., 2017; Ding et al., 2019; Ma et al., 2021). The commonly used open-source models in ECR are WRF-Chem and WRF-CMAQ (Grell et al., 2005; Wong et al., 2012), but there is no any application of the two-way coupled WRF-CHIMERE model that has been applied to examine aerosol-radiation-cloud interactions in Europe and Africa (Briant et al., 2017; Tuccella et al., 2019). At the same time, model simulations should be compared not only against surface measurement data but also satellite data (Zhao et al., 2017; Hong et al., 2017; Campbell et al., 2017; Wang et al., 2018). Even though the running time of an individual modeling system (e.g., WRF-CMAQ and WRF-CHIMERE) was evaluated by considering its online and offline versions and under various computing configurations (Wong et al., 2012; Briant et al., 2017), the computational efficiencies of multiple two-way coupled models need to be accessed under the same computing conditions as well.

In this paper, a comparative evaluation of three open-sourced two-way coupled meteorology and air quality models (WRF-CMAQ, WRF-Chem and WRF-CHIMERE) in ECR is conducted. The remainder of the paper is organized as follows: Section 2 describes the study methods including model configurations and evaluation protocols. Sections 3 and 4 presents the analyses and intercomparisons of simulations from these three two-way coupled models with regard to meteorology and air quality, respectively. The major findings of this work are summarized in Section 5.

2 Data and methods

2.1 Model configurations and data sources

One-year simulations of meteorology and air quality in eastern China were examined using the two-way coupled WRF–CMAQ, WRF–Chem, and WRF–CHIMERE models with and without enabling ARI and/or ACI, as well as with a 27 km horizontal grid resolution (the east–west direction comprised 110, 120, and 120 grid cells, and the north–south direction 150, 160, and 170 grid cells for the WRF–CMAQ, WRF–Chem, and WRF–CHIMERE models, respectively). All the three coupled models used in this study have 30 levels (i.e., 29 layers) from the surface to 100 hPa with 11 layers in the bottom 1 km and the bottom-layer thickness being 23.2 m. The anthropogenic emissions of Multiresolution Emission Inventory for China (MEIC) (Li et al., 2017) and the Fire INventory from NCAR, version 1.5 (FINN v1.5), biomass burning emissions (Wiedinmyer et al., 2011) were considered in our simulations, and their spatial, temporal, and species allocations were performed using Python (Wang et al., 2023). Biogenic emissions were calculated using the Model of Emissions of Gases and Aerosols from

Nature, version 3.0 (MEGAN v3.0; Gao et al., 2019). Dust and sea salt emissions were used in the calculations of the inline modules (Table 1). The meteorological ICs and lateral BCs were derived from the National Center for Environmental Prediction Final Analysis (NCEP-FNL) datasets (http://rda.ucar.edu/datasets/ds083.2), with a horizontal resolution of 1° × 1° at 6-hour intervals for each of the three coupled models, and the flux in the model-top boundary was set to zero. To improve the long-term accuracy of the meteorological variables when utilizing the WRF model, we turned on the options of observational and grid four-dimensional data assimilation (FDDA), and pressure, station height, relative humidity, wind speed (WS), and wind direction were observed four times per day at 00:00, 06:00, 12:00, and 18:00 UTC from 2,168 stations (https://doi.org/10.5281/zenodo.6975602, Gao et al., 2022). Notably, turning on FDDA in two-way coupled models could dampen the simulated aerosol feedback (Wong et al., 2012; Forkel et al., 2012; Hogrefe et al., 2015; Zhang et al., 2016). To mitigate the effects of turning on FDDA on aerosol feedback in long-term simulations, we set the nudging coefficients of the u/v wind, temperature, and water vapor mixing ratio above the planetary boundary layer to 0.0001, 0.0001, and 0.00001 s^{-1}, respectively. The chemical ICs/lateral BCs were downscaled from the whole atmosphere community climate model (WACCM) for WRF–CMAQ and WRF–Chem using the mozart2camx and mozbc tools, respectively. WRF–CHIMERE employed the climatology from a general circulation model developed at the Laboratoire de Météorologie Dynamique (LMDz) coupling a global chemistry and aerosol model INteractions between Chemistry and Aerosols (INCA; Mailler et al., 2017). For chemical model-top BCs, the WRF–CMAQ and WRF–Chem models consider the impacts of stratosphere–troposphere O_3 exchange using O_3-potential vorticity parameterization (Safieddine et al., 2014; Xing et al., 2016). The related options of both models were used in this study. WRF–CHIMERE employs the climatology from the LMDz–INCA data (Mailler et al., 2017).

Table 1 lists the options of parameterization schemes of aerosol–radiation–cloud interactions. To maintain the consistency of physical schemes, the same Rapid Radiative Transfer Model for General Circulation Models Applications (RRTMG) short-wave (SW) and long-wave (LW) radiation schemes and the Morrison microphysics scheme were adopted in the WRF–Chem and WRF–CMAQ models. WRF–CHIMERE applies the same radiation schemes, as well as the Thompson microphysics scheme. The other different schemes (cumulus, surface, and land surface) in the WRF–CMAQ and WRF–Chem models were selected, following Gao et al.'s (2022) widely utilized options outlined in Table S1. The other schemes employed in WRF–CHIMERE are the same as those in WRF–Chem. To consider the effects of clouds on radiative transfer calculations, the fractional cloud cover and cloud optical properties were included in the RRTMG SW/LW radiation schemes employed in the three coupled models (Xu and Randall, 1996; Iacono et al., 2008). The coupled WRF–CMAQ model with the Kain–Fritsch cumulus scheme included the impacts of cumulus cloud fraction (CF) on RRTMG radiation (Alapaty et al., 2012), whereas the WRF–Chem and WRF–CHIMERE models with the

Grell–Freitas cumulus scheme did not. In the Fast-JX photolysis scheme employed by the three coupled models, the impacts of clouds were included by considering the cloud cover and cloud optical properties. However, the calculations of the cloud cover and cloud optical properties differed in these models, and Table S1 presents the relevant information. Regarding the aerosol-size distribution, we used the modal approach with Aitken, accumulation, and coarse modes in WRF–CMAQ, as well as the 4 and 10 bin sectional approaches in the WRF–Chem and WRF–CHIMERE models, respectively (Binkowski and Roselle, 2003; Zaveri et al., 2008; Nicholls et al., 2014; Menut et al., 2013, 2016).

To demonstrate the capabilities of the three two-way coupled models with/without aerosol feedbacks in simulating meteorology and air quality, we comprehensively evaluated the strengths and weaknesses of each coupled model and validated them against extensive ground-based and satellite measurements. The ground-based data included 572 hourly ground-based meteorological observations (air temperature (T2) and relative humidity (RH2) at 2 m above the surface, WS at 10 m above the surface (WS10), and precipitation (PREC)) (http://data.cma.cn); 327 hourly national environmental observations [fine particulate matter ($PM_{2.5}$), ozone (O_3), nitrogen dioxide (NO_2), sulfur dioxide (SO_2), and carbon monoxide (CO)] (http://106.37.208.233:20035); 109 hourly surface SW radiation (SSR) measurements (Tang et al., 2019); and 74 radiosonde data retrieved two times per day, which used to calculate planetary boundary layer height at 08:00 and 20:00 local time (PBLH08 and PBLH12) (Guo et al., 2019). Figure 1 shows the locations of these data. Because there were no observed water vapor mixing ratio (w) data, this parameter was calculated by $w = \frac{rh}{w_s}$, where rh is the relative humidity and w_s is the saturation mixing ratio (Wallace and Hobbs, 2006).

The satellite data included the following: monthly average downwelling SW/LW flux at the surface and SW/LW flux at the top of the atmosphere (TOA) obtained from the clouds and the Earth's radiant energy system (CERES) (https://ceres.larc.nasa.gov); PREC from the Tropical Rainfall Measuring Mission (TRMM); CF, liquid-water path (LWP), and AOD from the Moderate Resolution Imaging Spectroradiometer (MODIS); tropospheric NO_2 and SO_2 columns in the planetary boundary layer (PBL) from the Ozone Monitoring Instrument; total CO column from the Measurements of Pollution in the Troposphere (https://giovanni.gsfc.nasa.gov/giovanni); total column ozone (TCO) from the Infrared Atmospheric Sounding Interferometer-Meteorological Operational Satellite-A (IASI-METOP-A) (https://cds.climate.copernicus.eu/cdsapp#!/dataset/satellite-ozone?tab=form); and total ammonia (NH_3) column from IASI-METOP-B (https://cds-espri.ipsl.fr/iasibl3/iasi_nh3/V3.1.0). These data were downloaded and interpolated to the same horizontal resolution as the model results using the Rasterio library (Gillies et al., 2013). Thereafter, the model and observed values at each grid point were extracted.

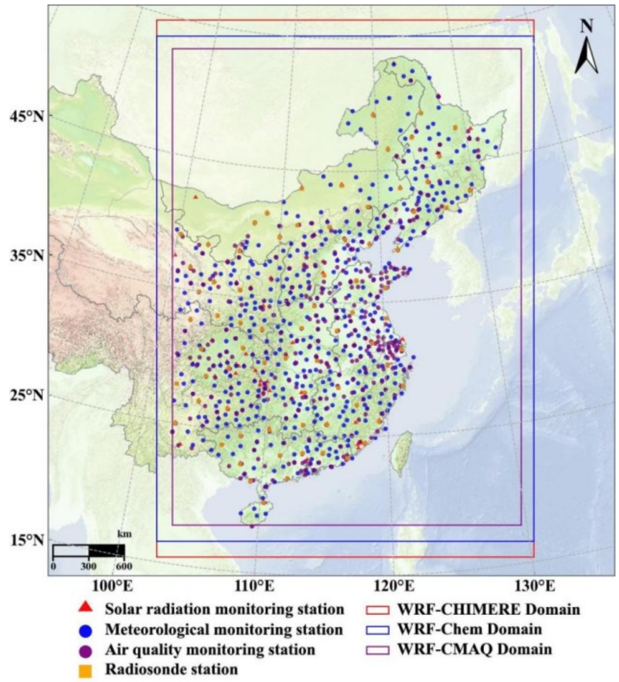

Figure 1. Modeling domains (WRF–CMAQ, WRF–Chem, and WRF–CHIMERE) and solar radiation, meteorology, air quality, and radiosonde stations.

Table 1. Model setups and inputs for the two-way coupled models (WRF–CMAQ, WRF–Chem, and WRF–CHIMERE).

		WRF-CMAQ	WRF-Chem	WRF-CHIMERE
Domain configuration	Horizontal grid spacing	27 km (110 × 150)	27 km (120 × 160)	27 km (120 × 170)
	Vertical resolution	30 levels	30 levels	30 levels
Physics parameterization	Shortwave radiation	RRTMG	RRTMG	RRTMG
	Longwave radiation	RRTMG	RRTMG	RRTMG
	Cloud microphysics	Morrison	Morrison	Thompson
	PBL	ACM2	YSU	YSU
	Cumulus	Kain-Fritsch	Grell-Freitas	Grell-Freitas
	Surface	Pleim-Xiu	Monin-Obukhov	Monin-Obukhov
	Land surface	Pleim-Xiu LSM	Noah LSM	Noah LSM
	Icloud	Xu-Randall method	Xu-Randall method	Xu-Randall method
Chemistry scheme	Aerosol mechanism	AERO6	MOSAIC	SAM
	Aerosol size distribution	Modal (3 modes)	Sectional (4 bins)	Sectional (10 bins)
	Aerosol mixing state	Core-Shell	Core-Shell	Core-Shell
	Gas-phase chemistry	CB6	CBMZ	MELCHIOR2
	Photolysis	Fast-JX with cloud effects	Fast-JX with cloud effects	Fast-JX with cloud effects
Emission	Anthropogenic emission	MEIC 2017	MEIC 2017	MEIC 2017
	Biogenic emission	MEGAN v3.0	MEGAN v3.0	MEGAN v3.0

	Biomass burning emission	FINN v1.5	FINN v1.5	FINN v1.5
	Dust emission	Foroutan	GOCART	Menut
	Sea-salt emission	Gong	Gong	Monahan
Input data	Meteorological ICs and BCs	FNL	FNL	FNL
	Chemical ICs and BCs	MOZART	MOZART	LMDZ-INCA

2.2 Scenario setup

To comprehensively assess the performances of WRF v4.1.1–CMAQ v5.3.1, WRF–Chem v4.1.1, and WRF v3.7.1–CHIMERE v2020r1 and performances affected by aerosol feedbacks over eastern China in 2017, eight sets of annual hindcast simulations with/without ARI and/or ACI were performed (Table 2). Compared with WRF v4.1.1–CMAQ v5.3.1 and WRF–Chem v4.1.1, this WRF v3.7.1–CHIMERE v2020r1 version can be officially obtained, and a higher version of WRF–CHIMERE has not been developed. Notably, the official WRF–Chem and WRF–CHIMERE can execute the simulation of ARI and ACI, whereas WRF–CMAQ cannot. In all of the simulations performed in this study, a spin-up time of one month was set up to reduce the influence of the initial conditions. Multiple statistical metrics, including the correlation coefficient (R), mean bias (MB), normalized mean bias (NMB), normalized gross error (NGE), and root mean square error (RMSE), were used between each scenario simulation and ground-based/satellite-borne observations. The mathematical definitions of these metrics are provided in Supplementary Information (SI) S1. To compare the simulations by the three coupled models, the respective model configurations of the physics and chemistry routines were set as consistent as possible. We systemically analyzed the annual and seasonal statistical metrics of the meteorological and air quality variables, including simulations by the three two-way coupled models with/without the ARI and/or ACI effects. Thereafter, we quantified the respective contributions of the ARI and ACI effects to model performance.

Table 2. Summary of scenario settings in the three coupled models.

Model	Scenario	Configuration option	Description
WRF-CMAQ	(1) WRF-CMAQ_NO	DO_SW_CAL=F	Without aerosol feedbacks
	(2) WRF-CMAQ_ARI	DO_SW_CAL=T	ARI
WRF-Chem	(3) WRF-Chem_NO	aer_ra_feedback=0	Without aerosol feedbacks
		wetscav_onoff=0	
		cldchem_onoff=0	
	(4) WRF-Chem_ARI	aer_ra_feedback=1	ARI
		wetscav_onoff=0	
		cldchem_onoff=0	
	(5) WRF-Chem_BOTH	aer_ra_feedback=1	ARI and ACI
		wetscav_onoff=1	

		cldchem_onoff=1	
WRF-CHIMERE	(6) WRF-CHIMERE_NO	direct_feed_chimere=0	Without aerosol feedbacks
		indirect_feed_chimere=0	
	(7) WRF-CHIMERE_ARI	direct_feed_chimere=1	ARI
		indirect_feed_chimere=0	
	(8) WRF-CHIMERE_BOTH	direct_feed_chimere=1	ARI and ACI
		indirect_feed_chimere=1	

3 Multimodel meteorological evaluations

This section presents the annual and seasonal (March–May, Spring; June–August, Summer; September–November, Autumn; and December–February, Winter) statistical metrics of the simulated meteorological variables and air quality, as well as their comparison with the ground-based and satellite observations. The running times of the eight simulation scenarios are also discussed.

3.1 Ground-based observations

Figures 2 and S1–S7 show the spatial distributions of R, MB, and RMSE for hourly SSR, T2, Q2, RH2, WS10, PREC, PBLH08, and PBLH120 from WRF–CMAQ, WRF–Chem, and WRF–CHIMERE with/without turning on aerosol feedback against ground-based observations from each site throughout 2017. The calculated annual model evaluation metrics for all sites in eastern China are summarized in Table S1, and the related seasonal R and MB values are presented in Fig. 3. Here, we mainly focused on the comparisons of SSR, T2, RH2, and WS10. Further, Section 1.1 of SI presents the analyses of PREC, PBLH08, and PBLH20.

The accuracy of radiation prediction is of great significance in ARI evaluation. The annual and seasonal average simulated SSR data were compared with the ground-based observations (Figs. 3–4 and Table S3), and SSR over eastern China was simulated very reasonably by the models, with R-values of 0.61–0.78. The simulated results were overestimated on the annual and seasonal scales (MBs in spring and summer were larger than those in autumn and winter). The overestimated annual SSRs were 19.98, 14.48, and 9.24 W m^{-2} for WRF–CMAQ, WRF–Chem, and WRF–CHIMERE, respectively. Brunner et al.'s (2015) comparative study also reported that most two-way coupled models overestimated SSR for Europe and North America. Such overestimations could be caused by multiple factors, namely, the uncertainties in cloud development owing to PBL and convection parameterizations (Alapaty et al., 2012) and the diversity in the treatment of land-surface processes (Brunner et al., 2015), which tend to play more important roles than the enabling of the two-way aerosol feedbacks on SSR through the effects of ARI and ACI. When the three models incorporated the ARI effects, the simulation accuracies for SSR over the whole year and four seasons improved, although the enabling of the ACI effects resulted in relatively limited improvement. Additionally, the MB variations of WRF–CMAQ and WRF–Chem simulations were higher in spring and winter than in summer and autumn, whereas the maximum and minimum MBs of WRF–CHIMERE simulations were obtained in summer (−10.33 W m^{-2}) and autumn (−7.64 W m^{-2}), respectively. The annual and seasonal decrease in SSR simulated by WRF–Chem and WRF–CHIMERE with enabled ACI effects were significantly smaller than those with enabled ARI effects.

Generally, the simulated magnitudes and temporal variations in the air temperature at 2 m above the ground exhibited high consistency with the observations (R = 0.88–0.97). Considering the annual and seasonal T2, the models tended to display a negative bias, and the T2 underestimations in spring and winter were greater than those in summer and autumn (Figs. 3 and 4). Following Makar et al. (2015a), WRF–Chem and GEM–MACH produced negative MBs in summer and positive MBs in winter with enabled ACI and ARI effects; additionally, WRF–CMAQ with only the ARI effects enabled produced negative MBs in summer over North America in 2010. Notably, Makar et al.'s. (2015a) study lacked winter meteorology evaluations using WRF–CMAQ. The comparison results of MBs revealed the following order: WRF–CHIMERE > WRF–CMAQ > WRF–Chem. The annual and seasonal MBs of WRF–CMAQ and WRF–Chem were approximately −1℃, whereas that of WRF–CHIMERE ranged from −2 to −1°C. The RMSE values of WRF–CMAQ (2.71–3.05°C) and WRF–Chem (2.82–3.27°C) were almost equal. Those of WRF–CHIMERE (3.39–4.53°C) were larger on the annual and seasonal scales. Notably, reduced underestimations of the annual and seasonal T2 by the three coupled models were observed in eastern China when the ARI effects were enabled. With the enabled ACI effects, the MBs for T2 simulated by WRF–Chem_BOTH did not change significantly compared with those of WRF–Chem_NO; additionally, compared with WRF–CHIMERE_NO, WRF–CHIMERE_BOTH further enhanced the underestimations of T2 in the full year (−1.30°C), spring (−0.12°C), and winter (−0.40°C).

Regarding RH2, the annual and seasonal simulations using WRF–CMAQ exhibited the highest correlation with the observed values, followed by WRF–Chem and WRF–CHIMERE, and the smallest correlation coefficients of the three models were observed in autumn (~0.5). The spatial MBs between the simulations using the three models and observations displayed a general converse trend compared with T2 (i.e., RH2 was overestimated where T2 was underestimated, and vice versa). This can be explained by calculating RH2 based on T2 in the models (Wang et al., 2021). The annual and seasonal MBs were 0.65%–71.03% and −21.30% to 60.00%, respectively (Fig. 4 and Table S3); only WRF–Chem produced negative MBs in the summer. The magnitude of RMSE exhibited an inverse pattern compared with R for the three models, with maximum (28.48%–29.52%) and minimum (12.57%–16.07%) values observed in autumn and summer, respectively. Figs. 3–4 and Table S3 show that WRF–CMAQ_ARI further reduced the overestimations of the annual and seasonal RH2 in ECR, whereas WRF–Chem_ARI (except for summer) and WRF–CHIMERE_ARI displayed the opposite trend. Moreover, the variations in the annual and seasonal RH2 MBs simulated by WRF–

Chem_BOTH and WRF–CHIMERE_BOTH were further reduced compared with those simulated by WRF–Chem_ARI (except for summer) and WRF–CHIMERE_ARI, respectively.

Furthermore, similar analyses were performed for WS10, and the results revealed that WRF–CMAQ performed better in capturing the WS10 patterns than WRF–Chem and WRF–CHIMERE. The R-values for all three models ranged from 0.47 to 0.60; WRF–CMAQ and WRF–Chem overestimated WS by ~0.5 m s^{-1}, whereas WRF–CHIMERE overestimated it by ~1.0 m s^{-1} (Table S3 and Figs. 3–4). The overestimation of WS10 under real-world low-wind conditions is a common phenomenon of existing weather models, and it is mainly caused by outdated geographic data, coarse model resolution, and a lack of good physical representation of the urban canopy (Gao et al., 2015, 2018). The three models exhibited lower correlations (0.31–0.54) and MBs (0.20–0.86 m s^{-1}) in summer compared with the other seasons, and the RMSEs were ~2.0 m s^{-1}. Enabling the ARI effects mitigated the overestimations of the three models, particularly WRF–CMAQ_ARI.

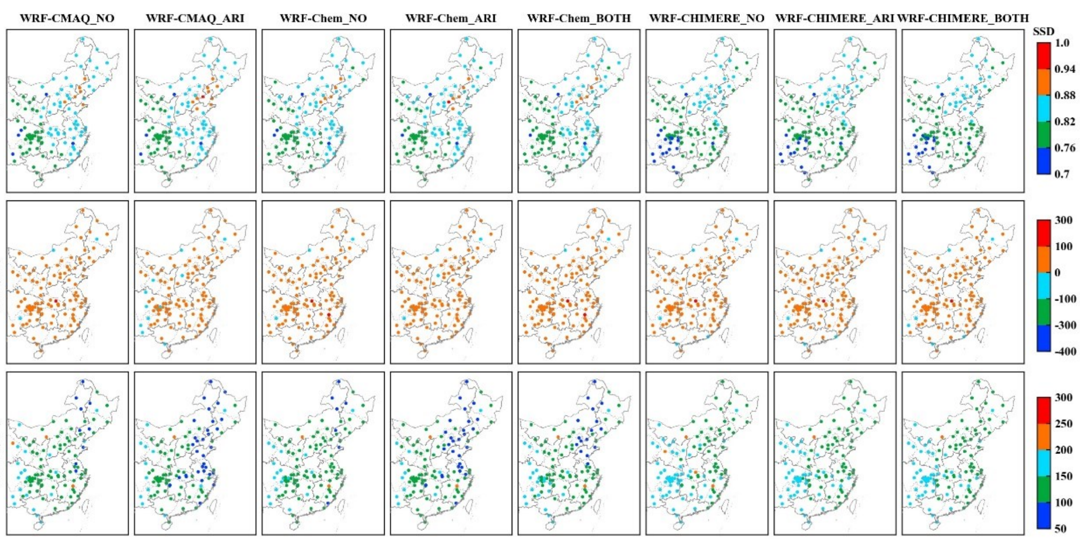

Figure 2. Statistical metrics (R, MB, and RMSE) for annual simulations and observations of SSR in eastern China.

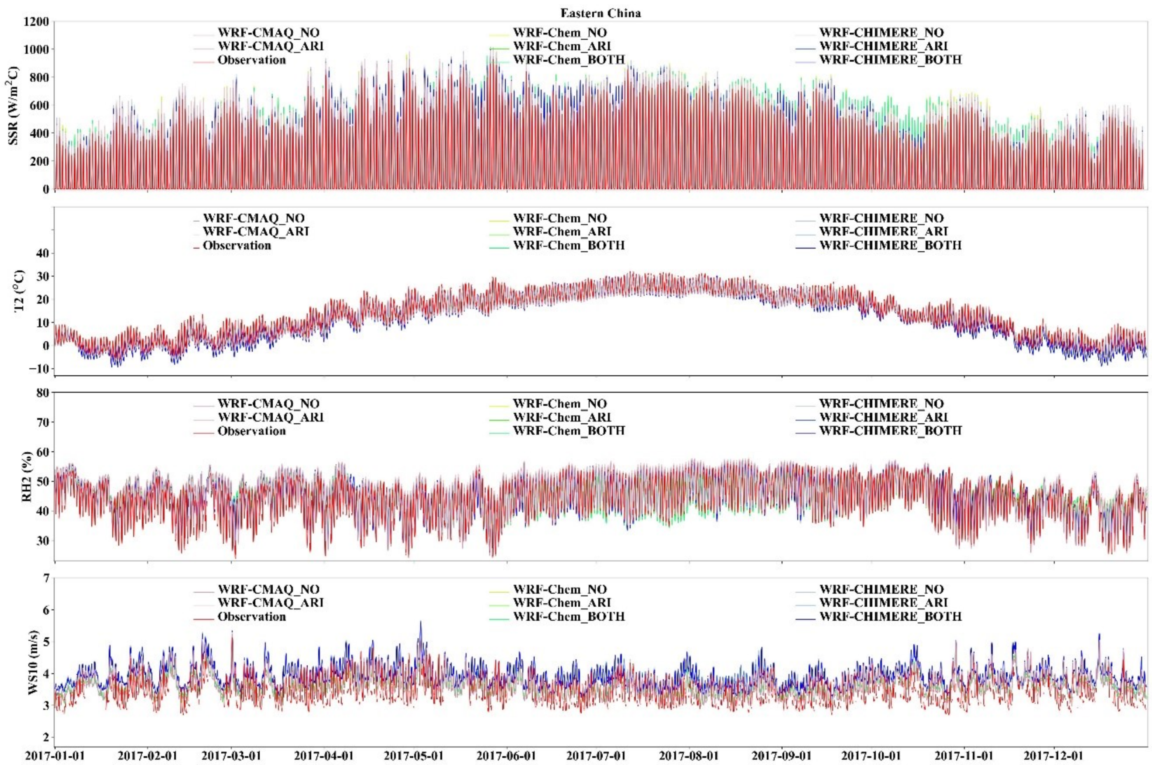

Figure 3. Time series of the observed and simulated hourly SSR, T2, RH2, and WS10 by coupled WRF–CMAQ, WRF–Chem, and WRF–CHIMERE with/without aerosol feedbacks over ECR in 2017.

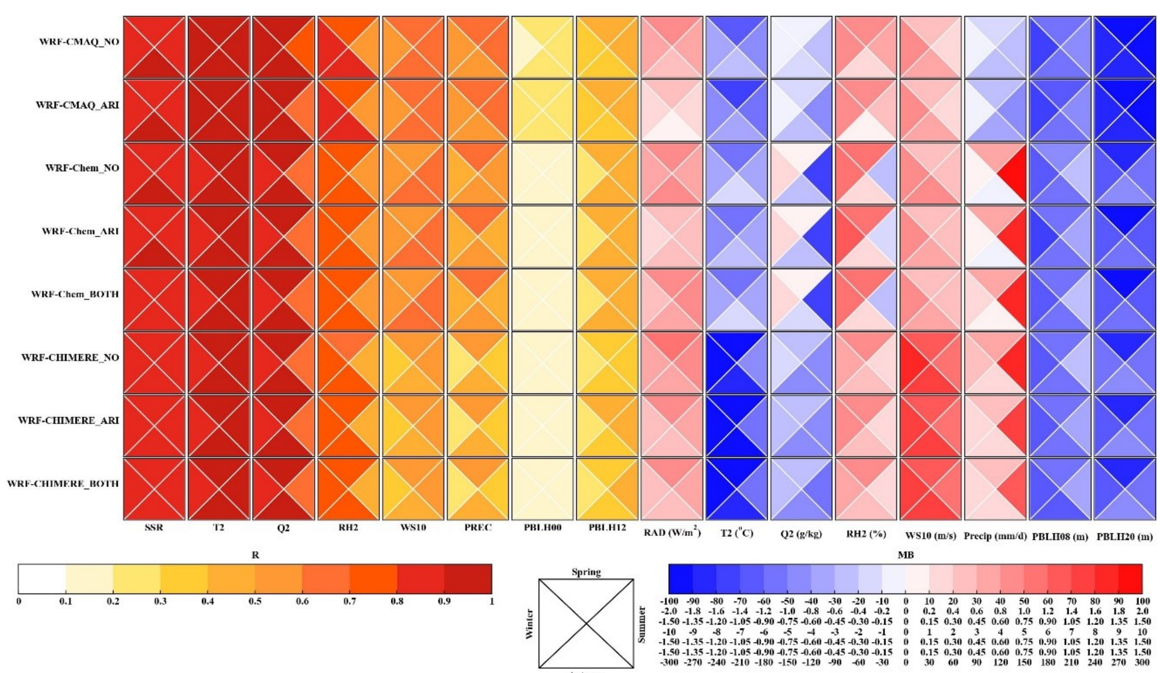

Figure 4. Portrait plots of the statistical indices (R and MB) between the seasonal simulations and

surface observations of the meteorological variables (SSR, T2, Q2, RH2, WS10, PREC, and PBLH at 08:00 and 20:00 LT) in ECR.

To determine and quantify how well our results compared with those of the extant studies using two-way coupled models, we compared our study with previous ones in terms of the evaluation results of meteorology and air quality. We discussed meteorology and air quality in this section and Section 4.1, respectively. We employed box-and-whisker plots, and the 5th, 25th, 75th, and 95th percentiles were used as statistical indicators. In the plots, the dashed lines in the boxes represent the mean values, and the circles represent outliers. Previous studies mainly used WRF–Chem and WRF–CMAQ to evaluate meteorology and air quality, whereas the WRF–NAQPMS and GRAPES–CUACE barely had application potential. As mentioned in Section 1, previous investigations of meteorology and air quality using WRF–CHIMERE with/without aerosol feedbacks have not been conducted in ECR. Therefore, only the evaluation results involving WRF–Chem and WRF–CMAQ were analyzed to study aerosol feedbacks.

Figure S8 shows the comparison between the statistical metrics, T2, RH2, Q2, and WS10, in this study and the evaluation results of previous studies. Based on the number of samples in the statistical metrics of each meteorological variable, most previous studies mainly involved the simulation and evaluation of T2, WS10, and RH2, with only a relatively few studies focusing on Q2. Compared with the evaluation results of the extant studies, the ranges of our statistical metrics were roughly similar, although there were some notable differences. The R-values of the WRF–CMAQ and WRF–Chem models in our study were higher than those of the previous studies; MBs of T2 simulated by WRF–CMAQ were smaller, whereas those of T2 simulated by WRF–Chem were larger; and RMSEs of the WRF–CMAQ simulation were larger, whereas those of the WRF–Chem simulation were smaller. For RH2, the R-values for our WRF–CMAQ and WRF–Chem were larger than the average level of the previous studies, whereas MBs and RMSEs for WRF–CMAQ were larger. Those for WRF–Chem were smaller than the average reported in previous studies. For Q2, the model performance of WRF–CMAQ in this study was generally better than the average level reported in previous studies, although the R-value between the WRF–Chem simulation results and observed values was higher (and MB and RMSE were lower) than the average level reported in previous studies. We also conclude that the simulation results of our WRF–CMAQ and WRF–Chem better reproduced the variations in WS10 compared with the simulation reported by previous studies.

3.2 Satellite-borne observations

To further evaluate the performances of WRF–CMAQ, WRF–Chem, and WRF–CHIMERE against the satellite observations, we analyzed the annual and seasonal statistical metrics of SW and LW radiations at the surface, PREC, cloud cover, and LWP simulated by the three coupled models with and without aerosol feedbacks by comparisons the simulations with the satellite-borne observations (Table 3 and Figs. 5, S9, and S12–S14). Additionally, evaluations of SW and LW radiation at TOA are presented in Section 1.2 of SI.

As shown in Table 3 and Fig. 5, the three coupled models exhibited relatively poor performances for SSR, with annual MBs of 8.21–30.74 W m^{-2} and correlations of 0.61–0.78. A similar poor performance for SW radiation was also reported in the United States using the coupled WRF–CMAQ and offline WRF models (Wang et al., 2021). The overall seasonal characteristics of SSR were reproduced by the three coupled models (Fig. S10). Concurrently, regardless of whether aerosol feedbacks were enabled or not, the three models overestimated seasonal SSR (except WRF–Chem_ARI in winter), obtaining higher MBs in spring and summer than in autumn and winter. The seasonal SSR overestimations might be directly due to the underestimation of the calculated AOD when examining the ARI effects (Wang et al., 2021). Compared with SSR, the three coupled models predicted the surface LW radiation variables (SLR) well (R-values were up to 0.99), with annual domain-average MBs of −9.97 to −6.05 W m^{-2}. Furthermore, significant seasonal differences were observed in the simulated LW radiation by the three coupled models; the WRF–CMAQ and WRF–CHIMERE scenarios yielded underestimations, with maximum and minimum SLR values in winter and summer, respectively, whereas the maximum underestimations of WRF–Chem were recorded in autumn, particularly for WRF–Chem_BOTH (Fig. S9).

As the three coupled models adopted the same grid resolution (27 × 27 km) as well as SW and LW radiation schemes (RRTMG), the above analysis demonstrated that the configuration differences among the aerosol components, size distributions, and mechanisms contributed to the diverse seasonal MBs (Tables 1 and S2). Moreover, the three two-way coupled models with ARI feedbacks effectively improved the performances of annual and seasonal SSR; however, for SLR, the performance improvements were much more variable across the three coupled models and different scenarios with and without ARI and/or ACI feedbacks enabled (Table S4). When the ARI effects were enabled, the diverse refractive indices of the aerosol species groups caused discrepancies in the online calculated aerosol optical properties in different SW and LW bands in the RRTMG SW/LW radiation schemes of WRF–CMAQ, WRF–Chem, and WRF–CHIMERE (Tables S5–S6). The online calculated cloud optical properties induced by aerosol absorption in the RRTMG radiation schemes differed regarding their treatments of the aerosol species groups in the three coupled models. With the ACI effects enabled, the activation of cloud droplets from aerosols based on the Köhler theory was considered in WRF–Chem and WRF–CHIMERE compared with the simulations without aerosol feedbacks (Table S7). The treatments of prognostic ice-nucleating particles (INP) formed via the heterogeneous nucleation of dust particles (diameters > 0.5 μm) and homogeneous freezing of hygroscopic aerosols (diameters > 0.1 μm) were only investigated in WRF–CHIMERE, whereas the prognostic INP were not included in WRF–CMAQ and WRF–Chem. These discrepancies eventually contributed to the differences in the simulated radiation changes caused by aerosols.

From IPCC 2007–2021, the effects of aerosol feedbacks (particularly with the ACI effects enabled) on PREC and cloud processes remained unclear. In this study, we further assessed the annual and seasonal simulated PREC, cloud cover, and LWP in ECR with high aerosol loadings against the satellite observations (Table 3 and Figs. S12–S14) to provide new insights into enabling online feedbacks in two-way coupled modeling simulations from a yearly perspective.

The results indicated that PREC simulated by WRF–CMAQ (0.51–0.89) exhibited higher correlations than those simulated by WRF–Chem (0.61–0.73) and WRF–CHIMERE (0.54–0.70). WRF–CMAQ demonstrated the best correlation in winter, whereas WRF–Chem and WRF–CHIMERE had the best correlation in spring; the three models presented their worst correlations in summer, as the numerical models struggled to effectively capture enhanced convective activities in summer. Huang and Gao (2018) also revealed that the accurate representations of lateral boundaries were crucial to improving PREC simulations in China during summer. WRF–CMAQ underestimated annual PREC, with MBs of −76.49 to −51.93 mm, whereas WRF–Chem and WRF–CHIMERE produced large PREC overestimations ranging from +108.04 to +207.05 mm (Table 3), particularly in southern China regions (Fig. S11). WRF–CMAQ also produced negative biases (−27.89 to +42.08 mm) for seasonal PREC, except for WRF–CMAQ_ARI in winter. WRF–Chem and WRF–CHIMERE only underestimated seasonal PREC in autumn (−31.39 to −26.89 mm) and winter (−7.12 to −4.43 mm), respectively (Fig. S12). The variations in the annual and seasonal MBs of PREC were consistent with the changes in CF and LWP (Zhang et al., 2016), and these changes will be discussed in detail below.

By considering aerosol feedbacks, the ARI-induced decrease in annual MBs of PREC for WRF–CMAQ, WRF–Chem, and WRF–CHIMERE were 24.56, 12.11, and 4.70 mm, respectively. WRF–Chem_BOTH (24.9 mm) and WRF–CHIMERE_BOTH (3.41 mm) enhanced the overestimation of annual PREC compared with WRF–Chem_ARI and WRF–CHIMERE_ARI, respectively. Significant increases (+53.15 mm) and decreases (−6.3 to −3.41 mm) in MBs were facilitated by WRF–CMAQ and the other two models with ARI effects enabled compared with those without feedbacks, respectively. WRF–Chem and WRF–CHIMERE with ARI and ACI effects enabled produced larger MB enhancements (+3.54 to +7.46 mm) on the seasonal scale (Fig. S12). Notably, the discrepancies in simulated PREC were mainly attributable to the selection of different microphysics and cumulus schemes in WRF–CMAQ (Morrison and Kain–Fritsch), WRF–Chem (Morrison and Grell–Freitas), and WRF–CHIMERE (Thompson and Grell–Freitas).

CF and LWP can significantly influence the spatiotemporal distributions of PREC; our simulated results of annual and seasonal CFs in ECR are presented in Table 3 and Fig. S13. Overall, WRF–CMAQ performed best in simulating CF. The R-values of WRF–Chem during summer (0.69) and winter (0.70) were larger than those of WRF–CMAQ (0.59 and 0.64) and WRF–CHIMERE (0.56 and 0.66), whereas WRF–CMAQ and WRF–

CHIMERE obtained better simulation results in winter and autumn, with correlations of up to 0.89 and 0.67, respectively. The three coupled models underestimated annual and seasonal CFs, with MBs of −16.83% to −6.18% and −21.13% to −4.13%, respectively; these results were consistent with those of previous two-way coupled modeling studies using WRF–CMAQ (−19.7%) and WRF–Chem (−32% to −9%) in China (Hong et al., 2017; Zhao et al., 2017). The models reasonably simulated the annual LWP in ECR, with R-values of >0.55 and negative biases varying from −57.36 to −31.29 g m^{-2}. These underestimations were closely related to missing cloud homogeneity (Wang et al., 2015; Dionne et al., 2020) and the excessive conversion of liquid water to ice in the selected cloud microphysics schemes (Klein et al., 2009). As shown in Fig. S14, the models performed best in simulating LWP in spring (R = 0.51–0.79), and their highest underestimations were observed in winter (MBs = −54.82 to −40.89 g m^{-2}), except for WRF–Chem, which obtained its maximum bias in autumn.

To quantitatively determine the impacts of aerosol feedbacks on CF and LWP, the simulated scenarios revealed that WRF–CMAQ_ARI overwhelmingly decreased the annual and seasonal underestimations of CF (0.48%–1.05%) and LWP (3.03–4.29 g m^{-2}), whereas in WRF–Chem_ARI and WRF–CHIMERE_ARI slightly increased the underestimations (CF: 0.02%–0.39%; LWP: 0.03–0.58 g m^{-2}). Compared with WRF–CHIMERE_ARI, WRF–CHIMERE_BOTH produced larger variations in the annual and seasonal MBs of CF (0.23%–0.93%) and LWP (−2.96 to 7.38 g m^{-2}). WRF–Chem_BOTH and WRF–Chem_ARI exhibited equivalent variations (CF: 0.03%–0.71%; LWP: 0.02–2.89 g m^{-2}). This could be explained by the different parameterization treatments of the cloud droplet number concentration (CDNC) simulated by the three coupled models with/without enabling the ACI effects. The cloud condensation nuclei (CCN) activated by the aerosol particles can increase CDNC and impact LWP and CF. Without enabling any aerosol feedbacks or by enabling only ARI, CDNC is, by default, prescribed as a constant value of 250 cm^{-3} in the Morrison schemes of WRF–CMAQ and WRF–Chem and 300 cm^{-3} in the Thompson schemes of WRF–CHIMERE. With enabling only ACI or both ARI and ACI effects, prognostic CDNC is online calculated in the two-way coupled WRF–Chem and WRF–CHIMERE models when cloud maximum supersaturation is greater than aerosol critical supersaturation (Abdul-Razzak and Ghan, 2002; Chapman et al., 2009; Tuccella et al., 2019). Although we have obtained preliminary quantitative results of the ACI effects on regional PREC, CF, and LWP, we acknowledge that several limitations still exist regarding the representation of the ACI effects in state-of-the-art two-way coupled models. These limitations include a lack of consideration for the responses of convective clouds to ACI (Tuccella et al., 2019), numerical descriptions for giant CCN (Wang et al., 2021) and heterogeneous ice nuclei (Keita et al., 2020).

Table 3. Statistical metrics (R, MB, NMB, NGE, and RMSE) between the annual simulations and satellite retrievals of SSR and SLR, TOA SW and LW radiation, PREC,

CF, and LWP in ECR. The best results are captured in bold fonts, and the mean simulations and observations are in italics.

Variables	Statistics	WRF-CMAQ_NO	WRF-CMAQ_ARI	WRF-Chem_NO	WRF-Chem_ARI	WRF-Chem_BOTH	WRF-CHIMERE_NO	WRF-CHIMERE_ARI	WRF-CHIMERE_BOTH
Surface shortwave radiation (*172.74* W m^{-2})	Mean_sim	*197.15*	*180.94*	*203.48*	*194.52*	*201.45*	*197.39*	*191.34*	*195.58*
	R	0.76	0.75	0.73	**0.78**	0.75	0.61	0.64	0.66
	MB	24.41	8.21	30.74	21.78	28.71	24.75	18.71	22.94
	NMB (%)	14.13	**4.75**	17.79	12.61	16.62	14.34	10.84	13.29
	NGE (%)	15.13	**8.66**	18.61	13.53	17.38	17.44	14.42	15.83
	RMSE	30.25	**20.37**	35.34	26.88	32.80	34.70	29.60	31.45
Surface longwave radiation (*322.3* W m^{-2})	Mean_sim	*316.25*	*315.83*	*312.96*	*312.60*	*312.32*	*313.33*	*314.60*	*314.47*
	R	0.98	0.98	0.98	0.98	0.98	**0.99**	**0.99**	**0.99**
	MB	-6.05	-6.46	-9.34	-9.70	-9.97	-9.66	-8.39	-8.53
	NMB (%)	**-1.88**	-2.00	-2.90	-3.01	-3.09	-2.99	-2.60	-2.64
	NGE (%)	**3.22**	3.46	3.70	3.77	3.84	3.96	3.60	3.66
	RMSE	**13.65**	14.13	14.81	14.97	15.17	15.47	14.52	14.72
TOA shortwave radiation (*111.56* W m^{-2})	Mean_sim	*107.76*	*112.68*	*110.38*	*110.95*	*107.16*	*114.33*	*116.62*	*113.09*
	R	**0.81**	0.79	0.69	0.68	0.62	0.65	0.65	0.65
	MB	-3.80	1.13	-1.18	-0.61	-4.40	3.12	5.42	1.89
	NMB (%)	-3.40	**1.01**	-1.05	-0.55	-3.94	2.81	4.87	1.70
	NGE (%)	**10.19**	10.45	11.52	10.96	11.69	14.43	14.36	12.93
	RMSE	**15.75**	16.04	17.07	16.10	17.21	20.85	20.67	18.96
TOA longwave radiation (*233.68* W m^{-2})	Mean_sim	*231.54*	*232.26*	*234.34*	*233.96*	*234.39*	*232.52*	*232.17*	*233.18*
	R	0.88	0.90	0.91	0.91	**0.92**	0.74	0.74	0.76
	MB	-2.14	-1.42	0.66	0.28	0.71	-0.61	-0.96	0.05
	NMB (%)	-0.92	-0.61	0.28	**0.12**	0.30	-0.26	-0.41	0.02
	NGE (%)	2.28	2.04	1.79	1.79	**1.74**	3.02	2.98	2.92
	RMSE	6.94	6.20	6.00	5.94	**5.86**	10.10	10.07	9.70
Precipitation (*948.91* mm y^{-1})	Mean_sim	*872.42*	*896.98*	*1069.06*	*1056.95*	*1081.84*	*1165.06*	*1160.35*	*1163.77*
	R	**0.71**	**0.71**	**0.71**	**0.71**	0.70	0.69	0.69	0.69
	MB	-76.49	-51.93	120.15	108.04	132.94	207.05	202.35	205.76
	NMB (%)	-9.23	**-8.40**	12.66	11.39	14.01	21.61	21.12	21.48
	NGE (%)	**32.46**	34.36	44.54	43.38	45.13	42.54	42.52	42.58
	RMSE	**573.14**	595.76	675.91	668.92	693.74	776.60	786.36	790.73
Cloud cover (*64.09* %)	Mean_sim	*52.51*	*53.32*	*48.18*	*47.80*	*47.46*	*58.12*	*57.98*	*58.55*
	R	0.68	0.68	**0.69**	**0.69**	0.68	0.66	0.66	0.64
	MB	-11.58	-10.77	-16.12	-16.50	-16.83	-6.60	-6.74	-6.18
	NMB (%)	-18.07	-16.80	-25.07	-25.66	-26.18	-10.20	-10.41	**-9.54**
	NGE (%)	19.48	18.87	26.01	26.56	26.97	16.74	16.92	**16.72**
	RMSE	16.47	16.28	20.17	20.48	20.73	15.28	15.33	15.34
liquid water path (*88.44*	Mean_sim	*53.50*	*57.15*	*32.29*	*31.87*	*31.08*	*56.23*	*56.21*	*54.00*
	R	**0.61**	0.58	0.47	0.46	0.28	0.55	0.55	0.51

g m^{-2})	MB	-34.94	-31.29	-56.16	-56.58	-57.36	-32.37	-32.40	-34.61
	NMB (%)	-39.51	**-35.38**	-63.49	-63.97	-64.86	-36.54	-36.56	-39.06
	NGE (%)	57.05	57.99	66.88	67.25	67.91	**53.15**	53.33	56.88
	RMSE	54.35	54.31	63.54	63.92	67.21	**53.39**	53.42	55.86

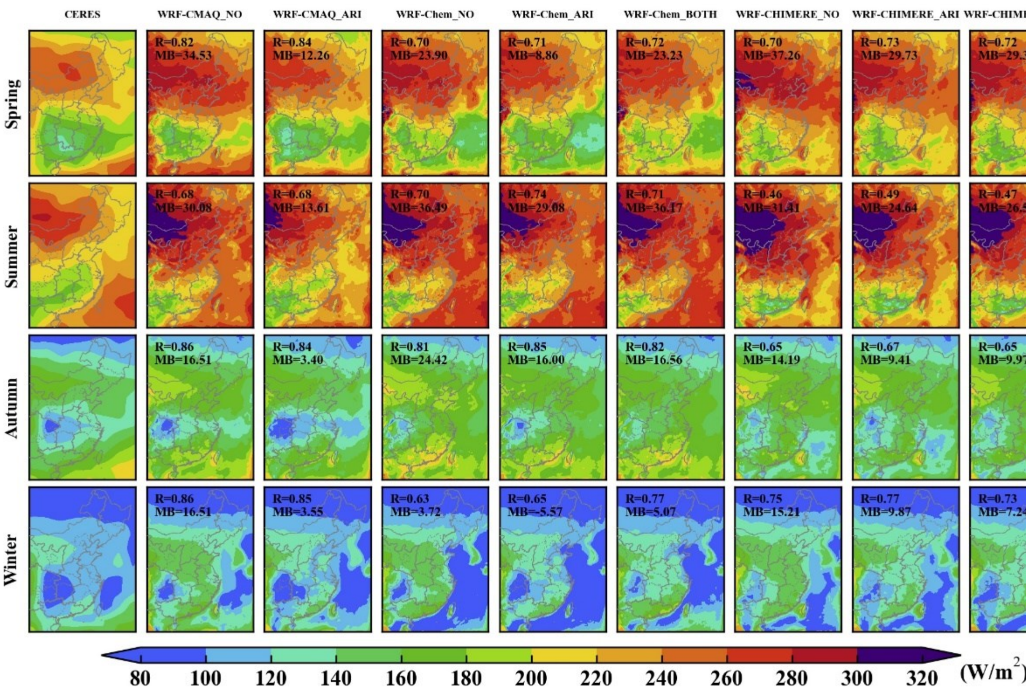

Figure 5. Spatial distributions of seasonal SSR between CERES observations and simulations using WRF–CMAQ, WRF–Chem, and WRF–CHIMERE with and without aerosol feedbacks in ECR.

4 Multimodel air-quality evaluations

Similar to meteorology, to further determine the quantitative effects of enabling aerosol feedbacks on the simulation accuracy of the air-quality variables in ECR, ground-based and satellite-borne observations were adopted for comparisons in the following evaluation analysis. The usage status of computing resources in each simulation process was also assessed (Section 4.3).

4.1 Ground-based observations

Table 4 and Fig. 7 present the statistical metrics of the annual and seasonal air pollutant concentrations ($PM_{2.5}$, O_3, NO_2, SO_2, and CO) simulated by the three coupled models. The evaluations between the surface measurements and simulations of $PM_{2.5}$ and O_3 are presented below, and the performance assessments of the other gaseous pollutants are presented in Section 2 of SI.

The R-values of the annual $PM_{2.5}$ concentrations simulated by WRF–CMAQ (0.68) were the highest, followed by those obtained by WRF–Chem (0.65–0.68) and WRF–

CHIMERE (0.52–0.53). The three models exhibited higher correlations in winter than in the other seasons (Fig. 7). Table 4 and Figs. 6–7 reveal that WRF–CMAQ underestimated the annual and seasonal (except for autumn) $PM_{2.5}$ concentrations, with NMBs of −9.78% to −6.39% and −17.68% to +5.17%, respectively. WRF–Chem overestimated and underestimated $PM_{2.5}$ on the annual and seasonal scales, with related NMBs varying from −39.11% to +24.72. Concurrently, WRF–CHIMERE excessively overestimated the annual and seasonal $PM_{2.5}$ concentrations (NMB: +19.51% to +75.47%). These biases could be related to the different aerosol and gas-phase mechanisms, dust and sea salt emission schemes, chemical ICs and BCs, and the aerosol-size-distribution treatments applied to the three two-way coupled models. Based on the NMB differences between the simulations with ARI and those without aerosol feedbacks, the ARI-induced annual and seasonal NMB variations in WRF–CMAQ_ARI and WRF–Chem_ARI ranged from +3.01% to +4.21% and +3.07% to +5.02%, respectively, indicating that enabling ARI feedbacks slightly reduced the annual and seasonal (except for autumn) underestimations of $PM_{2.5}$ concentrations. Notably, WRF–CHIMERE_ARI further overestimated the annual and seasonal $PM_{2.5}$ concentrations, with an NMB increase of up to 10.04%. The increases in the $PM_{2.5}$ concentrations due to the ARI effects were attributable to the synergetic decreases in SSR, T2, WS10, and PBLH, as well as increases in RH2. With ACI feedbacks further enabled, WRF–Chem_BOTH largely underestimated the annual and seasonal $PM_{2.5}$, with NMBs varying from −24.15% to −14.44%, compared with WRF–Chem_ARI. WRF–CHIMERE_BOTH tended to decrease (−2.1% to −0.51%) the annual and autumn–winter NMBs and increase (+0.35% to +3.04%) the spring–summer ones. A further comparison of the ARI- and ACI-induced NMB variations demonstrated that the ARI-induced variations in the $PM_{2.5}$ concentrations were smaller than the ACI-induced ones in WRF–Chem, and that the reversed pattern proceeded in WRF–CHIMERE. This might be explained by the incorporation of dust aerosols in WRF–CHIMERE serving as IN, which was not included in WRF–Chem in this study.

For O_3, WRF–CHIMERE (R = 0.62) exhibited the highest correlation, followed by WRF–CMAQ (R = 0.55) and WRF–Chem (R = 0.45) (Table 4 and Fig. S16). WRF–CMAQ slightly underestimated the annual O_3 concentration, with NMBs and NGEs of −12.57% to −11.52%; conversely, WRF–Chem and WRF–CHIMERE significantly overestimated it, with NMBs of 47.82%–48.10% and 29.46%–29.75%, respectively. The seasonal results of the statistical metrics displayed consistent patterns with the annual simulations, and the O_3 pollution levels in summer were better simulated than in the other seasons (Fig. 6). The models with enabling ARI feedbacks slightly decreased the annual and seasonal O_3 NMBs and NGEs, ranging from −3.02% to +0.85% (the only positive value of +0.85% was produced by WRF–CMAQ in summer) and −1.42% to −0.75%, respectively. Concurrently, regarding the ACI effects, WRF–Chem and WRF–CHIMERE exhibited increased annual O_3 NMBs and NGEs of 0.12%−0.65% and 0.40%−0.55%, respectively. The ACI-induced seasonal NMB variations for WRF–Chem differed from those for WRF–CHIMERE; WRF–Chem increased and decreased in spring–summer and autumn–winter, respectively, whereas WRF–CHIMERE increased in all seasons except winter (Fig. 7). Such diverse NMB and NGE variations can be explained by two aspect differences. Under the model-top BCs, the WRF–CMAQ and WRF–Chem models employed the parameterization scheme of O_3-potential vorticity, and WRF–CHIMERE employed the climatological data from LMDz–INCA. Regarding the gas-phase chemistry mechanisms, the three coupled models incorporated various photolytic reactions, with a more comprehensive discussion in Section 4.2.

Knote et al. (2015) comprehensively assessed the effects of seven gas-phase chemical mechanisms (RADM2, RADMKA, RACM-ESRL, CB05Clx, CB05-TUCL, CBMZ, and MOZART-4) on O_3 simulations using the three two-way coupled models (WRF–Chem, WRF–CMAQ, and COSMO–ART). They concluded that the O_3 concentrations simulated by WRF–Chem using the CBMZ mechanism were closest to the mean values of multiple models for North America and Europe in spring and summer. However, dissimilar to North America and Europe, the two-way coupled WRF–Chem with CBMZ exhibited the lowest performance in spring for ECR. Additionally, the ARI and/or ACI effects contributed to atmospheric dynamics and stability (as mentioned in the PBLH evaluation part of Section 1.1 in SI), as well as photochemistry and heterogeneous reactions; thus, they eventually influenced O_3 formation (Xing et al., 2017; Qu et al., 2021; Zhu et al., 2021).

Table 4. Statistical metrics (R, MB, NMB, NGE, and RMSE) of the annual simulations and observations of surface $PM_{2.5}$, O_3, NO_2, SO_2, and CO in ECR. The best results are in bold, while the mean simulations and observations are in italics.

Variables	Statistics	WRF-CMAQ_NO	WRF-CMAQ_ARI	WRF-Chem_NO	WRF-Chem_ARI	WRF-Chem_BOTH	WRF-CHIMERE_NO	WRF-CHIMERE_ARI	WRF-CHIMERE_BOTH
$PM_{2.5}$ (*44.99* μg m^{-3})	Mean_sim	*40.59*	*42.12*	*44.45*	*46.65*	*38.33*	*62.17*	*65.36*	*65.13*
	R	**0.68**	**0.68**	0.65	0.65	0.69	0.52	0.53	0.53
	MB	-4.40	-2.87	-0.54	1.66	-6.66	17.18	20.37	20.14
	NMB (%)	-9.78	-6.39	**-1.21**	3.69	-14.81	38.19	45.27	44.76
	NGE (%)	**46.41**	47.08	57.82	59.91	52.10	89.85	94.10	94.01
	RMSE	**27.62**	27.69	32.58	34.64	32.48	55.13	60.25	59.41
O_3 (*62.23* μg m^{-3})	Mean_sim	*55.06*	*54.41*	*88.53*	*87.81*	*87.89*	*76.92*	*76.48*	*76.89*
	R	0.54	0.55	0.46	0.45	0.45	**0.62**	**0.62**	**0.62**
	MB	-7.17	-7.83	26.30	25.58	25.65	14.69	14.25	14.66
	NMB (%)	**-11.52**	-12.57	42.26	41.10	41.22	23.60	22.90	23.55
	NGE (%)	**41.02**	41.40	87.02	86.17	86.57	58.17	57.63	58.18
	RMSE	**28.32**	28.68	48.10	47.99	47.82	29.65	29.46	29.75
NO_2 (*31.2* μg m^{-3})	Mean_sim	*33.94*	*34.46*	*21.17*	*21.98*	*21.40*	*21.85*	*22.20*	*22.24*
	R	0.59	**0.60**	0.50	0.50	0.50	0.55	0.56	0.56
	MB	2.74	3.26	-10.03	-9.22	-9.80	-9.35	-9.00	-8.96
	NMB (%)	**8.77**	10.44	-32.14	-29.55	-31.40	-29.96	-28.84	-28.73
	NGE (%)	55.04	55.74	54.57	54.37	54.43	50.56	**50.82**	50.89

	RMSE	**19.14**	19.48	21.23	21.21	21.21	18.72	18.68	18.70
SO_2	Mean_sim	*14.02*	*14.39*	*8.22*	*8.56*	*7.85*	*8.88*	*9.18*	*9.19*
(*18.51* μg m^{-3})	R	0.40	0.40	0.44	0.44	**0.46**	0.40	0.41	0.41
	MB	-4.49	-4.12	-10.29	-9.95	-10.66	-9.63	-9.33	-9.32
	NMB (%)	-24.25	**-22.24**	-55.61	-53.76	-57.57	-52.02	-50.39	-50.34
	NGE (%)	75.44	76.26	64.18	64.20	**66.09**	75.54	75.86	75.87
	RMSE	21.11	21.30	20.13	**20.02**	20.20	22.07	22.17	22.18
CO	Mean_sim	*0.44*	*0.45*	*0.53*	*0.54*	*0.53*	*0.56*	*0.58*	*0.57*
(*0.96* mg m^{-3})	R	0.23	0.24	0.21	0.22	0.22	0.47	**0.48**	0.47
	MB	-0.52	-0.51	-0.43	-0.42	-0.43	-0.40	-0.39	-0.39
	NMB (%)	-53.97	-52.99	-45.10	-43.94	-44.68	-41.82	**-40.11**	-40.28
	NGE (%)	65.44	65.11	53.63	53.38	53.80	47.27	**47.08**	47.09
	RMSE	0.90	0.90	0.82	0.83	0.83	**0.62**	**0.62**	**0.62**

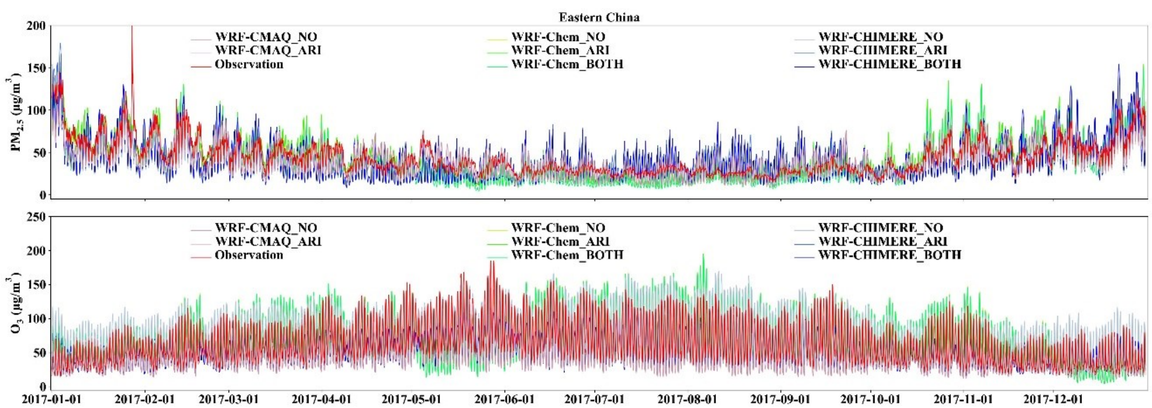

Figure 6. Time series of the observed and simulated hourly $PM_{2.5}$ and O_3 concentrations by WRF–CMAQ, WRF–Chem, and WRF–CHIMERE with/without aerosol feedbacks over ECR in 2017.

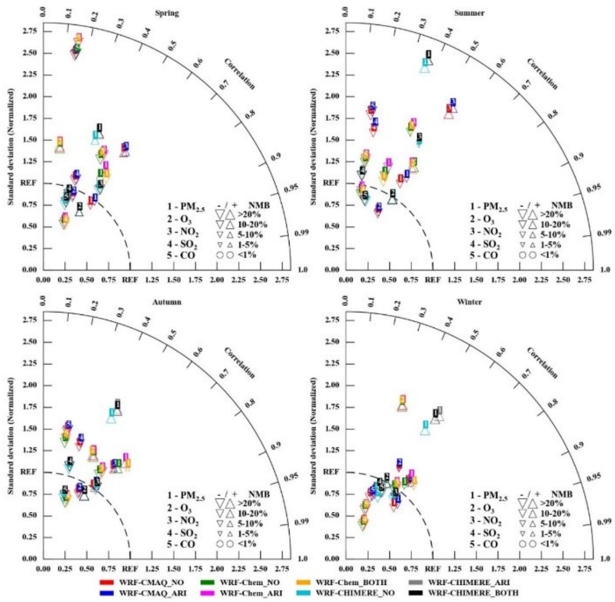

Figure 7. Taylor diagrams (R, normalized standard deviation, and NMB) of seasonal $PM_{2.5}$, O_3, NO_2, SO_2, and CO using the three two-way coupled models (WRF–CMAQ, WRF–Chem, and WRF–CHIMERE) with/without the ARI and/or ACI effects in ECR compared with the surface observations

Similar to the meteorological variables presented above, we conducted quality assurance for the statistical metrics via further comparisons with the $PM_{2.5}$ and O_3 results in previous model evaluations (Fig. S20). In this study, the performances of WRF–CMAQ and WRF–Chem in simulating $PM_{2.5}$ were better than the average levels reported by the previous studies on ECR. Regarding the simulation of the O_3 level, WRF–Chem performed worse compared with the average level reported by the previous studies. Although the R-values of O_3 simulated by WRF–CMAQ in this study were lower than the average level reported in the previous studies, our RMSEs were smaller.

4.2 Satellite-borne observations

In this section, we further investigated the discrepancies among the different models regarding the calculated AOD and column concentrations of the gases (O_3, NO_2, SO_2, CO, and NH_3) and compared them with various satellite observations. Regarding NH_3, as the output of simulated NH_3 concentrations was not set in WRF–CHIMERE, the discussion here only includes the results from the WRF–CMAQ and WRF–Chem models.

Table 5 reveals that the annual AOD at 550 nm, TCO, NO_2, and CO simulated by the three models agreed the most with the satellite observations, with R-values of 0.80–0.98; these were followed by NH_3 (0.75–0.76), and SO_2 (0.50–0.53). WRF–CMAQ exhibited negative biases for the annual AOD (−0.01), TCO (−5.92 Dobson Units (DU)), SO_2 (−0.03 to −0.02 DU), CO (-1.25×10^{17} molecules cm^{-2}), and NH_3 (-2.95×10^{15} molecules cm^{-2}). Conversely, it exhibited a positive bias for NO_2 (1.09–1.21 petamolecules cm^{-2}). Regarding AOD, WRF–Chem and WRF–CHIMERE produced positive (+0.09) and negative (−0.06) MBs. WRF–Chem and WRF–CHIMERE overestimated NO_2 (0.28–0.63 petamolecules cm^{-2}) and CO ($0.93–1.21 \times 10^{17}$ molecules

cm^{-2}) and underestimated O_3 (−10.99 to −3.63 DU) and SO_2 (−0.03 to −0.02 DU). Similar to WRF–CMAQ, WRF–Chem underestimated NH_3 by approximately -3.14×10^{15} molecules cm^{-2}.

Regarding the seasonal variations, we observed relatively high correlation relationships (0.71–0.88) regarding AOD in autumn, with lower values (0.53–0.84) in the other seasons (Fig. 8). WRF–CMAQ and WRF–Chem tended to underestimate (MBs of −0.1 to −0.4) and overestimate (MBs of 0.01–0.05) AOD in summer and the other seasons, respectively. WRF–CHIMERE exhibited positive (0.03–0.04) and negative (−0.10 to −0.01) biases in winter and the other seasons, respectively. Regarding TCO (Fig. S24), the performances of the WRF–CMAQ and WRF–Chem models in spring and winter were slightly better than the performances in summer and autumn; however, the R-values of all the seasons were above 0.89. WRF–CMAQ (−9.53 to −0.72 DU) and WRF–Chem (−24.62 to +10.57 DU) exhibited negative biases in all the seasons (except WRF–Chem in autumn). WRF–CHIMERE better captured TCO in spring and summer (overestimations of +9.19 to +29.20 DU) than in autumn and winter (underestimations of −33.75 to −19.40 DU). The R-values of the NO_2 columns for the three models were slightly higher in autumn and winter (0.82–0.91) than in spring and summer (0.76–0.84). Generally, WRF–CMAQ (−0.68 to −0.16 DU), WRF–Chem (−1.40 to −0.44 DU), and WRF–CHIMERE (−1.31 to −0.19 DU) generally underestimated the seasonal NO_2 columns (Fig. S22). All the models overestimated the SO_2 column concentrations in winter (by 0.01–0.03 DU) but underestimated them in the other seasons (−0.05 to −0.001 DU) (Fig. S23). Regarding NH_3, the only primary alkaline gas in the atmosphere, the WRF–CMAQ and WRF–Chem models performed better in summer (R: 0.81–0.87; MB: -3.42 to 2.07×10^{15} molecules cm^{-2}) (Fig. S25). The NH_3 emissions from fertilizers and livestock have been substantially underestimated in China (Zhang et al., 2017), and the peak values were obtained in spring and summer (Huang et al., 2012). Additionally, the bidirectional exchanges of fertilizer-induced NH_3 were not considered in our simulations. Compared with the above column variables, WRF–CMAQ, WRF–Chem, and WRF–CHIMERE exhibited relatively poor performances (R: 0.68–0.79) in simulating the CO columns during spring, summer, and autumn, respectively, than in simulating them in the other seasons (Fig. S24). WRF–CMAQ and WRF–CHIMERE underestimated and overestimated the CO columns in the other seasons, respectively, except for summer and spring, with MBs of -3.29 to 0.31×10^{17} and -0.62 to 2.09×10^{17} molecules cm^{-2}, respectively. WRF–Chem obtained positive MBs in summer and autumn (4.03–5.12×10^{17} molecules cm^{-2}) and negative ones in spring and winter (-3.15 to -2.10×10^{17} molecules cm^{-2}).

Moreover, after comparing the performances of the models for each pollutant between Sections 4.1 and 4.2, the only disparity found between evaluations with ground-based observations and those with satellite-borne observations was for CO. The formation of CO via the oxidation of methane, an important source of CO emissions (Stein et al., 2014), was not considered in the three coupled models, and the methane emissions were not included in the MEIC inventory. Furthermore, the contribution of CO to atmospheric oxidation capacity (OH radicals) was nonnegligible (e.g., the values were approximately 20.54%–38.97% in Beijing (Liu et al., 2021) and 26%–31% in Shanghai (Zhu et al., 2020)). In addition, these discrepancies in the model performances in simulating AOD and column concentrations of gases can be explained by the differences in the representations of the aerosol species groups, Fast-JX photolysis scheme, and gas-phase mechanisms in the three coupled models. More detailed interpretations were grouped into four aspects: (1) AODs are calculated via the Mie theory using the refractive indices of different numbers (5, 6, and 10) of aerosol species groups in different coupled models (WRF–CMAQ, WRF–Chem, and WRF–CHIMERE) (Tables S5–S6); (2) seven (294.6, 303.2, 310.0, 316.4, 333.1, 382.0, and 607.7 nm), four (300, 400, 600, and 999 nm), and five (200, 300, 400, 600, and 999 nm) effective wavelengths were used to calculate the actinic fluxes and photolysis rates in the Fast-JX photolysis modules of WRF–CMAQ, WRF–Chem, and WRF–CHIMERE, respectively; (3) different methods exist in the Fast-JX schemes of the three coupled models for calculating the aerosol and cloud optical properties (Tables S1 and S5–S6); (4) 77, 52, and 40 gas-phase species comprised 218, 132, and 120 gas-phase reactions under the CB6, CBMZ, and MELCHIOR2 mechanisms, respectively.

When the three models enabled only the ARI effects, relatively limited improvements were observed in the annual AOD and NO_2 columns simulated by these models. The AOD simulations improved in spring and summer but worsened in autumn and winter (Table 4 and Fig. 9). Larger ARI-induced variations in seasonal MBs of the NO_2 columns were observed in WRF–CMAQ (−0.18 to 0.13 petamolecules cm^{-2}) compared with WRF–Chem and WRF–CHIMERE (0–0.01 petamolecules cm^{-2}). When the ARI and ACI effects were enabled in WRF–Chem, the model performance for seasonal AOD simulations worsened considerably. The annual and seasonal NO_2 simulations by WRF–Chem became slightly worse, whereas those by WRF–CHIMERE became slightly better. Dissimilar to AOD and the NO_2 column concentrations, the improvements in the annual and seasonal column simulations of total ozone, PBL SO_2, and NH_3 by all the two-way coupled models were limited when one or both of ARI and ACI were enabled.

Table 5. Statistical metrics (R, MB, NMB, NGE, and RMSE) of the simulated and satellite-retrieved AOD, TCO, tropospheric column NO_2, PBL column SO_2, total column CO, and total column density of NH_3 in ECR. The best results are captured in bold fonts, and the annual mean simulations and observations are in italics.

Variables	Statistics	WRF-CMAQ_NO	WRF-CMAQ_ARI	WRF-Chem_NO	WRF-Chem_ARI	WRF-Chem_BOTH	WRF-CHIMERE_NO	WRF-CHIMERE_ARI	WRF-CHIMERE_BOTH
AOD (*0.27*)	Mean_sim	*0.26*	*0.27*	*0.35*	*0.36*	*0.25*	*0.21*	*0.22*	*0.22*
	R	0.80	0.80	0.80	0.80	0.75	**0.87**	**0.87**	0.86
	MB	-0.01	-0.01	0.09	0.09	-0.01	-0.05	-0.05	-0.04
	NMB (%)	-3.99	**-2.93**	34.14	35.03	-4.92	-18.72	-17.37	-16.22
	NGE (%)	34.90	34.82	58.21	58.89	41.46	32.15	**32.11**	32.06

	RMSE	**0.09**	**0.09**	0.15	0.15	0.10	**0.09**	**0.09**	0.10
O_3 VCDs (*312.07* DU)	Mean_sim	*306.15*	*306.15*	*300.77*	*300.73*	*300.46*	*307.69*	*307.47*	*307.75*
	R	**0.98**	**0.98**	0.97	0.97	0.97	0.65	0.65	0.65
	MB	-5.92	-5.92	-10.68	-10.72	-10.99	-3.69	-3.91	-3.63
	NMB (%)	-1.90	-1.90	-3.43	-3.44	-3.53	-1.19	-1.26	**-1.17**
	NGE (%)	**2.46**	**2.46**	25.02	25.02	25.08	10.95	10.89	10.93
	RMSE	**8.91**	**8.91**	83.72	83.73	83.94	39.88	39.71	39.73
Tropospheric NO_2 VCDs (2.71×10^{15} molecules cm^{-2})	Mean_sim	*3.80*	*3.91*	*3.07*	*3.08*	*3.06*	*2.62*	*2.63*	*2.63*
	R	0.85	0.85	**0.87**	**0.87**	**0.87**	**0.87**	**0.87**	**0.87**
	MB	1.09	1.21	0.62	0.63	0.61	0.28	0.29	0.29
	NMB (%)	40.35	44.64	25.27	25.52	24.89	**12.03**	12.47	12.42
	NGE (%)	52.80	55.08	46.01	46.05	**45.17**	46.06	46.31	46.24
	RMSE	3.18	3.33	2.27	2.27	2.27	**1.65**	1.67	1.68
PBL SO_2 VCDs (*0.09* DU)	Mean_sim	*0.07*	*0.07*	*0.09*	*0.09*	*0.06*	*0.06*	*0.06*	*0.06*
	R	0.53	0.53	**0.56**	**0.56**	0.54	0.50	0.50	0.50
	MB	-0.03	-0.02	-0.03	-0.02	-0.03	-0.03	-0.02	-0.02
	NMB (%)	-27.32	-25.48	-32.50	**-21.50**	-35.08	-28.64	-27.31	-27.51
	NGE (%)	**57.45**	58.26	67.55	68.07	64.83	68.31	68.61	68.80
	RMSE	**0.07**	**0.07**	0.08	0.08	**0.07**	**0.07**	**0.07**	**0.07**
Total CO VCDs (21.60×10^{17} molecules cm^{-2})	Mean_sim	*20.34*	*20.35*	*22.20*	*22.20*	*22.21*	*22.34*	*22.36*	*22.35*
	R	0.83	0.83	**0.87**	**0.87**	**0.87**	0.86	0.86	0.86
	MB	-1.26	-1.24	0.93	0.93	0.94	1.19	1.21	1.19
	NMB (%)	-5.83	-5.75	**4.35**	4.37	4.44	5.64	5.70	5.65
	NGE (%)	9.33	**9.31**	10.30	10.28	10.32	11.02	11.06	11.10
	RMSE	**2.54**	**2.54**	2.69	2.68	2.69	2.57	2.58	2.58
Total NH_3 VCDs (16.05×10^{15} molecules cm^{-2})	Mean_sim	*13.06*	*13.15*	*12.31*	*12.27*	*8.63*	N/A	N/A	N/A
	R	**0.76**	**0.76**	0.73	0.73	0.76	N/A	N/A	N/A
	MB	-3.00	-2.90	-3.27	-3.32	-3.34	N/A	N/A	N/A
	NMB (%)	-18.66	**-18.08**	-21.01	-21.28	-21.41	N/A	N/A	N/A
	NGE (%)	**47.69**	48.09	50.84	50.80	50.99	N/A	N/A	N/A
	RMSE	**9.26**	9.47	9.48	9.46	9.61	N/A	N/A	N/A

N/A indicates that the outputs of the NH_3 column concentrations were not extracted from WRF–CHIMERE simulations with/without aerosol feedbacks.

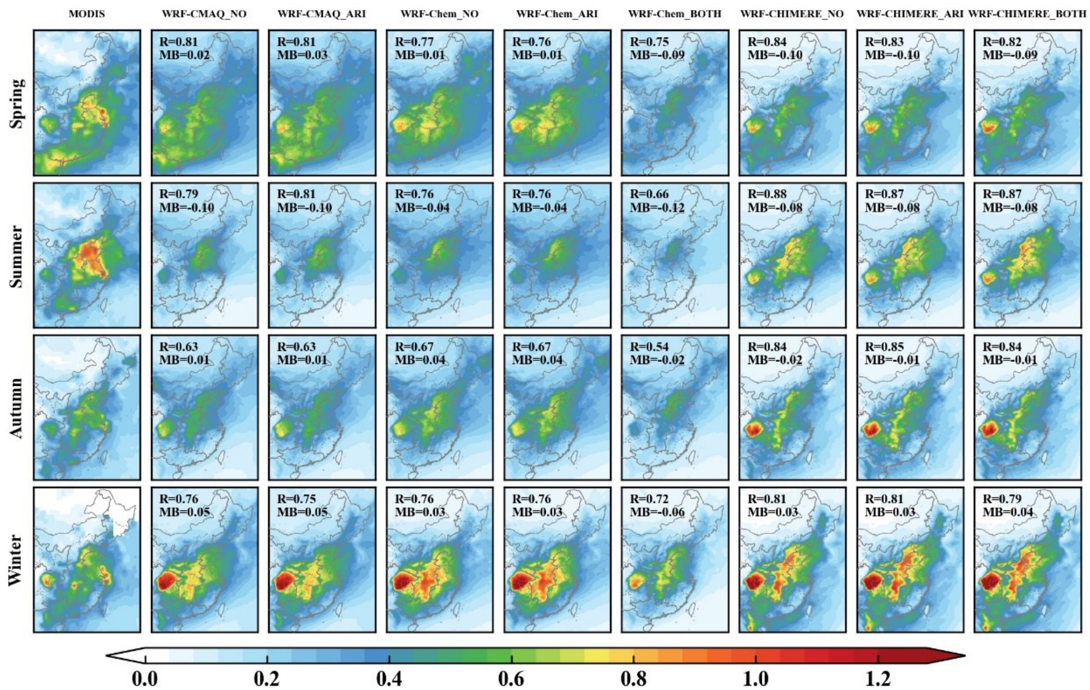

Figure 8. Spatial distributions of seasonal AOD between MODIS observations and simulations using the WRF–CMAQ, WRF–Chem, and WRF–CHIMERE models with and without aerosol feedbacks in ECR.

4.3 Computational performance

Table 5 presents a summary of the comparative results of the time consumption by the central processing unit (CPU) per simulation day using WRF–CMAQ, WRF–Chem, and WRF–CHIMERE with and without aerosol feedbacks in 2017. The results indicated that WRF–CMAQ consumed the shortest CPU time simulating one-day meteorology and air quality with or without enabling aerosol feedbacks. This CPU time consumption was followed by WRF–CHIMERE and WRF–Chem. Compared with the simulations without aerosol feedbacks, the processing time of WRF–CMAQ with ARI increased by 0.22–0.34 h per day. The increases in the running time of WRF–Chem and WRF–CHIMERE were insignificant (0.02–0.03 h per day). The CPU times for WRF–Chem and WRF–CHIMERE with the ARI and ACI effects enabled increased slightly, and the increase in the CPU time for the former (0.25 h per day) was higher than that for the latter (0.11 h per day). Compared with WRF–CMAQ and WRF–Chem, the CPU time consumed by WRF–CHIMERE exhibited clear seasonal differences, with the CPU times in winter and spring being significantly longer than those in summer and autumn. These differences can be partially explained by the choice of the main configurations, including the model resolution, model version, and parametrization schemes (cloud microphysics, PBL, cumulus, surface layer, land surface, gas-phase chemistry, and aerosol mechanisms).

Table 5. Summary of the running time for the different coupled models.

Month	WRF–CMAQ (h)		WRF–Chem (h)			WRF–CHIMERE (h)		
	NO	ARI	NO	ARI	BOTH	NO	ARI	BOTH
Jan.	0.37	0.59	0.69	0.71	0.96	0.67	0.70	0.77
Feb.	0.35	0.60	0.68	0.70	0.93	0.64	0.67	0.73
Mar.	0.39	0.65	0.70	0.72	1.00	0.59	0.62	0.72
Apr.	0.37	0.67	0.67	0.69	0.92	0.54	0.57	0.65
May	0.39	0.71	0.61	0.66	0.86	0.52	0.55	0.62
June	0.40	0.74	0.66	0.67	0.95	0.48	0.51	0.63
July	0.36	0.69	0.65	0.67	0.86	0.49	0.50	0.58
Aug.	0.38	0.68	0.66	0.68	0.90	0.49	0.52	0.61
Sept.	0.37	0.63	0.64	0.65	0.89	0.48	0.52	0.63
Oct.	0.38	0.62	0.66	0.68	0.94	0.53	0.56	0.69
Nov.	0.36	0.58	0.68	0.70	0.91	0.64	0.67	0.72
Dec.	0.35	0.57	0.63	0.66	0.87	0.67	0.70	0.74

5 Conclusions

Two-way coupled meteorology and air-quality models have been deployed in ECR in recent years. However, no study comprehensively assessed multiple coupled models in this region. To the best of our knowledge, this is the first study to perform comprehensive intercomparisons of the open-sourced two-way coupled meteorology and air-quality models (WRF–CMAQ, WRF–Chem, and WRF–CHIMERE). Here, we systemically evaluated the hindcast simulations for 2017 and explored the impacts of ARI and/or ACI on the model performance and computational efficiency in ECR.

After detailed comparisons with ground-based and satellite-borne observations, the evaluation results revealed that the three coupled models performed well for meteorology and air quality, particularly for surface temperature (with an R-value of up to 0.97) and $PM_{2.5}$ concentrations (with an R-value of up to 0.68). The effects of aerosol feedbacks on the model performance varied with the two-way coupled models, variables, and time scales. The computational time increased by 20%–70% when these two-way coupled models enabled aerosol feedbacks compared with when the simulations proceeded without aerosol–radiation–cloud interactions. Notably, the three coupled models could effectively reproduce the spatiotemporal distributions of the satellite-retrieved CO column concentrations but not for ground-observed CO concentrations.

The intercomparisons revealed some uncertainty sources in the evaluation of the aerosol feedback effects. As numerous schemes can be combined with the configurations of different coupled models, we only evaluated the simulations with specific settings. Future comparisons considering more combinations of multiple schemes within the same or different coupled models are desired. Among the three coupled models, the numerical representations for specific variables in the same scheme are diverse, e.g., the treatments of cloud cover and cloud optical properties in the Fast-JX photolysis scheme. More accurate representations of photolysis processes must be considered to reduce evaluation uncertainties. Additionally, the FDDA nudging technique can attenuate the ARI effects during severe air pollution episodes, and optimal nudging coefficients among different regions must be determined. Finally, the actual mechanisms underlying the ACI effects are still unclear, and the new advances in the measurements and parameterizations of CCN/IN activations and PREC must be duly incorporated in coupled models.

Code availability

The source codes of the two-way coupled WRF v4.1.1-CMAQ v5.3.1, WRF-Chem v4.1.1, and WRF v3.7.1-CHIMERE v2020r1 models are obtained from https://github.com/USEPA/CMAQ, https://github.com/wrf-model/WRF, and https://www.lmd.polytechnique.fr/chimere, respectively (last access: November 2020). The related source codes, configuration information, namelist files and automated run scripts of these three two-way coupled models are archived at Zenodo with the associated DOI: https://doi.org/10.5281/zenodo.7901682 (Gao et al., 2023a; link: https://zenodo.org/record/7901682).

Data availability

The meteorological ICs and BCs used for three coupled models can be obtained at https://doi.org/10.5281/zenodo.7925012 (Gao et al., 2023b; link: https://zenodo.org/record/7925012). The Chemical ICs and BCs used for WRF-CMAQ, WRF-Chem and WRF-CHIMERE are available at https://doi.org/10.5281/zenodo.7932390 (Gao et al., 2023c; link: https://zenodo.org/record/7932390), https://doi.org/10.5281/zenodo.7932936 (Gao et al., 2023d; link: https://zenodo.org/record/7932936), and https://doi.org/10.5281/zenodo.7933641 (Gao et al., 2023e; link: https://zenodo.org/record/7933641), respectively. The emission data used for WRF-CMAQ, WRF-Chem and WRF-CHIMERE can be downloaded from https://doi.org/10.5281/zenodo.7932430 (Gao et al., 2023f; link: https://zenodo.org/record/7932430), https://doi.org/10.5281/zenodo.7932734 (Gao et al., 2023g; link: https://zenodo.org/record/7932734), and https://doi.org/10.5281/zenodo.7931614 (Gao et al., 2023h; link: https://zenodo.org/record/7931614), respectively. The DOIs and links regarding the output data of each simulation scenario are presented in Table S9. All data used to create figures and tables in this study are provided in an open repository on Zenodo (https://doi.org/10.5281/zenodo.7750907, Gao et al., 2023i; link: https://zenodo.org/record/7750907).

Author contributions

CG, ZX, AX performed the majority of the source code configuration of WRF-CMAQ, WRF-Chem and WRF-CHIMERE, designed the numerical simulations to carry them out, related analysis, figure plotting, and paper writing. QT, HZ, SZ, GY, MZ and XS were involved with the original research plan and made suggestions for the paper writing.

Competing interests

The contact author has declared that neither they nor their co-authors have any competing interests.

Acknowledgements

The authors are very grateful to David Wong, Chun Zhao and Laurent Menut who provided detailed information on the two-way coupled WRF-CMAQ, WRF-Chem and WRF-CHIMERE models, respectively.

Financial support

This study was financially sponsored by the National Natural Science Foundation of China (grant nos. 42305171, 42371154 & 42171142), the Youth Innovation Promotion Association of Chinese Academy of Sciences, China (grant nos. 2022230), the National Key Research and Development Program of China (grant nos. 2017YFC0212304 & 2019YFE0194500), the Talent Program of Chinese Academy of Sciences (Y8H1021001), and the Natural Science Foundation of Jilin Province (YDZJ202201ZYTS476).

References

Abdul-Razzak, H. and Ghan, S. J.: A parameterization of aerosol activation 3. Sectional representation, J. Geophys. Res. Atmos., 107, AAC-1, https://doi.org/10.1029/2001JD000483, 2002.

Alapaty, K., Herwehe, J. A., Otte, T. L., Nolte, C. G., Bullock, O. R., Mallard, M. S., Kain, J. S., and Dudhia, J.: Introducing subgrid-scale cloud feedbacks to radiation for regional meteorological and climate modeling, Geophys. Res. Lett., 39, 1–5, https://doi.org/10.1029/2012GL054031, 2012.

Archer-Nicholls, S., Lowe, D., Utembe, S., Allan, J., Zaveri, R. A., Fast, J. D., Hodnebrog, Ø., Denier Van Der Gon, H., and Mcfiggans, G.: Gaseous chemistry and aerosol mechanism developments for version 3.5.1 of the online regional model, WRF-Chem, Geosci. Model Dev., 7, 2557–2579, https://doi.org/10.5194/gmd-7-2557-2014, 2014.

Baklanov, A., Schlünzen, K., Suppan, P., Baldasano, J., Brunner, D., Aksoyoglu, S., Carmichael, G., Douros, J., Flemming, J., and Forkel, R.: Online coupled regional meteorology chemistry models in Europe: current status and prospects, Atmos. Chem. Phys., 14, 317–398, https://doi.org/10.5194/acp-14-317-2014, 2014.

Balzarini Briant, R., Tuccella, P., Deroubaix, A., Khvorostyanov, D., Menut, L., Mailler, S., and

Turquety, S.: Aerosol-radiation interaction modelling using online coupling between the WRF 3.7.1 meteorological model and the CHIMERE 2016 chemistry-transport model, through the OASIS3-MCT coupler, Geosci. Model Dev., 10, 927–944, https://doi.org/10.5194/gmd-10-927-2017, 2017.

Briant, R., Tuccella, P., Deroubaix, A., Khvorostyanov, D., Menut, L., Mailler, S., and Turquety, S.: Aerosol-radiation interaction modelling using online coupling between the WRF 3.7.1 meteorological model and the CHIMERE 2016 chemistry-transport model, through the OASIS3-MCT coupler, Geosci. Model Dev., 10, 927–944, https://doi.org/10.5194/gmd-10-927-2017, 2017.

Brunner, D., Savage, N., Jorba, O., Eder, B., Giordano, L., Badia, A., Balzarini, A., Baro, R., Bianconi, R., and Chemel, C.: Comparative analysis of meteorological performance of coupled chemistry-meteorology models in the context of AQMEII phase 2, Atmos. Environ., 115, 470–498, https://doi.org/10.1016/j.atmosenv.2014.12.032, 2015.

Campbell, P., Zhang, Y., Wang, K., Leung, R., Fan, J., Zheng, B., Zhang, Q., and He, K.: Evaluation of a multi-scale WRF-CAM5 simulation during the 2010 East Asian Summer Monsoon, Atmos. Environ., 169, 204–217, https://doi.org/10.1016/j.atmosenv.2017.09.008, 2017.

Carslaw, K. S., Boucher, O., Spracklen, D. V, Mann, G. W., Rae, J. G. L., Woodward, S., and Kulmala, M.: A review of natural aerosol interactions and feedbacks within the Earth system, Atmos. Chem. Phys., 10, 1701–1737, https://doi.org/10.5194/acp-10-1701-2010, 2010.

Chapman, E. G., Jr, W. I. G., Easter, R. C., Barnard, J. C., Ghan, S. J., Pekour, M. S., and Fast, J. D.: and Physics Coupling aerosol-cloud-radiative processes in the WRF-Chem model : Investigating the radiative impact of elevated point sources, 945–964, https://doi.org/10.5194/acp-9-945-2009, 2009.

Chen, L., Gao, Y., Zhang, M., Fu, J. S., Zhu, J., Liao, H., Li, J., Huang, K., Ge, B., and Wang, X.: MICS-Asia III: Multi-model comparison and evaluation of aerosol over East Asia, Atmos. Chem. Phys., 19, 11911–11937, https://doi.org/10.5194/acp-19-11911-2019, 2019.

Ding, Q. J., Sun, J., Huang, X., Ding, A., Zou, J., Yang, X., and Fu, C.: Impacts of black carbon on the formation of advection–radiation fog during a haze pollution episode in eastern China, Atmos. Chem. Phys., 19, 7759–7774, https://doi.org/10.5194/acp-19-7759-2019, 2019.

Dionne, J., von Salzen, K., Cole, J., Mahmood, R., Leaitch, W. R., Lesins, G., Folkins, I., and Chang, R. Y.-W.: Modelling the relationship between liquid water content and cloud droplet number concentration observed in low clouds in the summer Arctic and its radiative effects, Atmos. Chem. Phys., 20, 29–43, https://doi.org/10.5194/acp-20-29-2020, 2020.

Fan, J., Wang, Y., Rosenfeld, D., and Liu, X.: Review of aerosol-cloud interactions: Mechanisms, significance, and challenges, J. Atmos. Sci., 73, 4221–4252, https://doi.org/10.1175/JAS-D-16-0037.1, 2016.

Feng, X., Lin, H., Fu, T.-M., Sulprizio, M. P., Zhuang, J., Jacob, D. J., Tian, H., Ma, Y., Zhang, L., and Wang, X.: WRF-GC (v2.0): online two-way coupling of WRF (v3.9.1.1) and GEOS-Chem (v12.7.2) for modeling regional atmospheric chemistry–meteorology interactions, Geosci. Model Dev., 14, 3741–3768, https://doi.org/10.5194/gmd-14-3741-2021, 2021.

Forkel, R., Werhahn, J., Hansen, A. B., McKeen, S., Peckham, S., Grell, G., and Suppan, P.: Effect of aerosol-radiation feedback on regional air quality–A case study with WRF/Chem, Atmos. Environ., 53, 202–211, https://doi.org/10.1016/j.atmosenv.2011.10.009,

Gao, C., Zhang, X., Xiu, A., Huang, L., Zhao, H., Wang, K., and Tong, Q.: Spatiotemporal distribution of biogenic volatile organic compounds emissions in China, Acta Sci. Circumstantiae, 39, 4140–4151, https://doi.org/10.13671/j.hjkxxb.2019.0243, 2019.

Gao, C., Xiu, A., Zhang, X., Tong, Q., Zhao, H., Zhang, S., Yang, G., and Zhang, M.: Two-way coupled meteorology and air quality models in Asia: a systematic review and meta-analysis of impacts of aerosol feedbacks on meteorology and air quality, Atmos. Chem. Phys., 22, 5265–5329, https://doi.org/10.5194/acp-22-5265-2022, 2022.

Gao, C., Xiu, A., Zhang, X.: Oservational data for sfdda nudging analysis in WRF model over China during 2017, Zenodo [Data set], https://doi.org/10.5281/zenodo.6975602, 2022.

Gao, C., Xiu, A., Zhang, X., Tong, Q., Zhao, H., Zhang, S., Yang, G., Zhang, M., Xie, S.: Source codes of WRF v4.1.1-CMAQ v5.3.1, WRF-Chem v4.1.1 and WRF v3.7.1-CHIMERE v2020r1, Zenodo [software]. https://doi.org/10.5281/zenodo.7901682, 2023a.

Gao, C., Xiu, A., Zhang, X., Tong, Q., Zhao, H., Zhang, S., Yang, G., Zhang, M., Xie, S.: FNL data used for producing meteorological ICs/BCs of WRF v4.1.1-CMAQ v5.3.1, WRF-Chem v4.1.1 and WRF v3.7.1-CHIMERE v2020r1, Zenodo [data set], https://doi.org/10.5281/zenodo.7925012, 2023b.

Gao, C., Xiu, A., Zhang, X., Tong, Q., Zhao, H., Zhang, S., Yang, G., Zhang, M., Xie, S.: Chemical initial and boundary conditions for WRF-CMAQ, Zenodo [data set], https://doi.org/10.5281/zenodo.7932390, 2023c.

Gao, C., Xiu, A., Zhang, X., Tong, Q., Zhao, H., Zhang, S., Yang, G., Zhang, M., Xie, S.: Chemical initial and boundary conditions for WRF-Chem. Zenodo [data set], https://doi.org/10.5281/zenodo.7932936, 2023d.

Gao, C., Xiu, A., Zhang, X., Tong, Q., Zhao, H., Zhang, S., Yang, G., Zhang, M., Xie, S.: Chemical initial and boundary conditions for WRF-CHIMERE, Zenodo [data set], https://doi.org/10.5281/zenodo.7933641, 2023e.

Chao Gao, Xuelei Zhang, Aijun Xiu, Qingqing Tong, Hongmei Zhao, Shichun Zhang, Guangyi Yang, Mengduo Zhang, Shengjin Xie: Emission input data for WRF-CMAQ, Zenodo [data set], https://doi.org/10.5281/zenodo.7932430, 2023f.

Gao, C., Xiu, A., Zhang, X., Tong, Q., Zhao, H., Zhang, S., Yang, G., Zhang, M., Xie, S.: Emission input data for WRF-Chem, Zenodo [data set], https://doi.org/10.5281/zenodo.7932734, 2023g.

Gao, C., Xiu, A., Zhang, X., Tong, Q., Zhao, H., Zhang, S., Yang, G., Zhang, M., Xie, S.: Emission input data for WRF-CHMIERE, Zenodo [data set], https://doi.org/10.5281/zenodo.7931614, 2023h.

Gao, C., Xiu, A., Zhang, X., Tong, Q., Zhao, H., Zhang, S., Yang, G., Zhang, M., Xie, S.: Data used to create figures and tables in the GMD manuscript "Inter-comparison of multiple two-way coupled meteorology and air quality models (WRF v4.1.1-CMAQ v5.3.1, WRF-Chem v4.1.1 and WRF v3.7.1-CHIMERE v2020r1) in eastern China", Zenodo [data set], https://doi.org/10.5281/zenodo.7750907, 2023i.

Gao, J., Woodward, A., Vardoulakis, S., Kovats, S., Wilkinson, P., Li, L., Xu, L., Li, J., Yang, J., and Cao, L.: Haze, public health and mitigation measures in China: A review of the current evidence for further policy response, Sci. Total Environ., 578, 148–157, https://doi.org/10.1016/j.scitotenv.2016.10.231, 2017.

Gao, M., Han, Z., Liu, Z., Li, M., Xin, J., Tao, Z., Li, J., Kang, J. E., Huang, K., Dong, X., Zhuang, B., Li, S., Ge, B., Wu, Q., Cheng, Y., Wang, Y., Lee, H. J., Kim, C. H., Fu, J. S., Wang, T., Chin, M., Woo, J. H., Zhang, Q., Wang, Z., and Carmichael, G. R.: Air quality and climate change, Topic 3 of the Model Inter-Comparison Study for Asia Phase III (MICS-Asia III)- Part 1: Overview and model evaluation, Atmos. Chem. Phys., 18, 4859–4884, https://doi.org/10.5194/acp-18-4859-2018, 2018.

Gao, M., Han, Z., Tao, Z., Li, J., Kang, J.-E., Huang, K., Dong, X., Zhuang, B., Li, S., and Ge, B.: Air quality and climate change, Topic 3 of the Model Inter-Comparison Study for Asia Phase III (MICS-Asia III)–Part 2: aerosol radiative effects and aerosol feedbacks, Atmos. Chem. Phys., 20, 1147–1161, https://doi.org/10.5194/acp-20-1147-2020, 2020.

Gao, Y., Zhang, M., Liu, Z., Wang, L., Wang, P., Xia, X., Tao, M., and Zhu, L.: Modeling the feedback between aerosol and meteorological variables in the atmospheric boundary layer during a severe fog-haze event over the North China Plain., Atmos. Chem. Phys., 15, 4279–4295, https://doi.org/10.5194/acp-15-4279-2015, 2015.

Ge, B., Itahashi, S., Sato, K., Xu, D., Wang, J., Fan, F., Tan, Q., Fu, J. S., Wang, X., and Yamaji, K.: Model Inter-Comparison Study for Asia (MICS-Asia) phase III: multimodel comparison of reactive nitrogen deposition over China, Atmos. Chem. Phys., 20, 10587–10610, https://doi.org/10.5194/acp-20-10587-2020, 2020.

Geng, G., Zheng, Y., Zhang, Q., Xue, T., Zhao, H., Tong, D., Zheng, B., Li, M., Liu, F., and Hong, C.: Drivers of PM2.5 air pollution deaths in China 2002–2017, Nat. Geosci., 14, 645–650, https://doi.org/10.1038/s41561-021-00792-3, 2021.

Gillies, S., Ward, B., and Petersen, A. S.: Rasterio: Geospatial raster I/O for Python programmers, URL https//github.com/mapbox/rasterio, 2013.

Govardhan, G. R., Nanjundiah, R. S., Satheesh, S. K., Moorthy, K. K., and Takemura, T.: Inter-comparison and performance evaluation of chemistry transport models over Indian region, Atmos. Environ., 125, 486–504, https://doi.org/10.1016/j.atmosenv.2015.10.065, 2016.

Grell, G. and Baklanov, A.: Integrated modeling for forecasting weather and air quality: A call for fully coupled approaches, Atmos. Environ., 45, 6845–6851, https://doi.org/10.1016/j.atmosenv.2011.01.017, 2011.

Grell, G. A., Peckham, S. E., Schmitz, R., McKeen, S. A., Frost, G., Skamarock, W. C., and Eder, B.: Fully coupled “online” chemistry within the WRF model, Atmos. Environ., 39, 6957–6975, https://doi.org/10.1016/j.atmosenv.2005.04.027, 2005.

Guo, J., Li, Y., Cohen, J. B., Li, J., Chen, D., Xu, H., Liu, L., Yin, J., Hu, K., and Zhai, P.: Shift in the temporal trend of boundary layer height in China using long-term (1979-2016) radiosonde data, Geophys. Res. Lett., 46, 6080–6089, https://doi.org/10.1029/2019GL082666, 2019.

He, K., Huo, H., and Zhang, Q.: Urban air pollution in China: current status, characteristics, and progress, Annu. Rev. Environ. Resour., 27, 397, https://doi.org/10.1146/annurev.energy.27.122001.083421, 2002.

Hogrefe, C., Bash, J. O., Pleim, J. E., Schwede, D. B., Gilliam, R. C., Foley, K. M., Appel, K. W., and Mathur, R.: An Analysis of CMAQ Gas Phase Dry Deposition over North America Through Grid-Scale and Land-Use Specific Diagnostics in the Context of AQMEII4, Atmos. Chem. Phys. Discuss., 1–52, https://doi.org/10.5194/acp-2023-10, 2023.

Hong, C., Zhang, Q., Zhang, Y., Tang, Y., Tong, D., and He, K.: Multi-year downscaling application of two-way coupled WRF v3.4 and CMAQ v5.0.2 over east Asia for regional climate and air quality modeling: model evaluation and aerosol direct effects., Geosci. Model Dev., 10, 2447–2470, https://doi.org/10.5194/gmd-10-2447-2017, 2017.

Huang, D. and Gao, S.: Impact of different reanalysis data on WRF dynamical downscaling over China, Atmos. Res., 200, 25–35, https://doi.org/10.1016/j.atmosres.2017.09.017, 2018.

Huang, X., Song, Y., Li, M., Li, J., Huo, Q., Cai, X., Zhu, T., Hu, M., and Zhang, H.: A high-resolution ammonia emission inventory in China, Global Biogeochem. Cycles, 26, https://doi.org/10.1029/2011GB004161, 2012.

Iacono, M. J., Delamere, J. S., Mlawer, E. J., Shephard, M. W., Clough, S. A., and Collins, W. D.: Radiative forcing by long‐lived greenhouse gases: Calculations with the AER radiative transfer models, J. Geophys. Res. Atmos., 113, https://doi.org/10.1029/2008JD009944, 2008.

Im, U., Bianconi, R., Solazzo, E., Kioutsioukis, I., Badia, A., Balzarini, A., Baró, R., Bellasio, R., Brunner, D., and Chemel, C.: Evaluation of operational on-line-coupled regional air quality models over Europe and North America in the context of AQMEII phase 2. Part I: Ozone, Atmos. Environ., 115, 404–420, https://doi.org/10.1016/j.atmosenv.2014.09.042, 2015a.

Im, U., Bianconi, R., Solazzo, E., Kioutsioukis, I., Badia, A., Balzarini, A., Baró, R., Bellasio, R., Brunner, D., and Chemel, C.: Evaluation of operational online-coupled regional air quality models over Europe and North America in the context of AQMEII phase 2. Part II: Particulate matter, Atmos. Environ., 115, 421–441, https://doi.org/10.1016/j.atmosenv.2014.08.072, 2015b.

IPCC: Climate change 2007: Synthesis Report. Contribution of Working Groups I, II and III to the Fourth Assessment Report of the Intergovernmental Panel on Climate Change, 2007.

IPCC: Climate change 2021: Synthesis Report. Contribution of Working Groups I, II and III to the Sixth Assessment Report of the Intergovernmental Panel on Climate Change., 2021.

Itahashi, S., Ge, B., Sato, K., Fu, J. S., Wang, X., Yamaji, K., Nagashima, T., Li, J., Kajino, M., and Liao, H.: MICS-Asia III: overview of model intercomparison and evaluation of acid deposition over Asia, Atmos. Chem. Phys., 20, 2667–2693, https://doi.org/10.5194/acp-20-2667-2020, 2020.

Jacobson, M. Z.: Developing, coupling, and applying a gas, aerosol, transport, and radiation model to study urban and regional air pollution, 1994.

Jacobson, M. Z.: Development and application of a new air pollution modeling system—Part III. Aerosol-phase simulations, Atmos. Environ., 31, 587–608, https://doi.org/10.1016/S1352-2310(96)00201-4, 1997.

Jacobson, M. Z.: Studying the effects of aerosols on vertical photolysis rate coefficient and temperature profiles over an urban airshed, J. Geophys. Res. Atmos., 103, 10593–10604, https://doi.org/10.1029/98jd00287, 1998.

Jacobson, M. Z.: GATOR-GCMM: A global-through urban-scale air pollution and weather forecast model: 1. Model design and treatment of subgrid soil, vegetation, roads, rooftops, water, sea ice, and snow, J. Geophys. Res. Atmos., 106, 5385–5401, https://doi.org/10.1029/2000JD900560, 2001.

Jacobson, M. Z.: Analysis of aerosol interactions with numerical techniques for solving coagulation, nucleation, condensation, dissolution, and reversible chemistry among multiple size distributions, J. Geophys. Res. Atmos., 107, AAC-2, https://doi.org/10.1029/2001JD002044, 2002.

Keita, S. A., Girard, E., Raut, J.-C., Leriche, M., Blanchet, J.-P., Pelon, J., Onishi, T., and Cirisan, A.: A new parameterization of ice heterogeneous nucleation coupled to aerosol chemistry in WRF-Chem model version 3.5.1: evaluation through ISDAC measurements, Geosci. Model Dev., 13, 5737–5755, https://doi.org/10.5194/gmd-13-5737-2020, 2020.

Klein, S. A., McCoy, R. B., Morrison, H., Ackerman, A. S., Avramov, A., Boer, G. de, Chen, M., Cole, J. N. S., Del Genio, A. D., and Falk, M.: Intercomparison of model simulations of mixed-phase clouds observed during the ARM Mixed-Phase Arctic Cloud Experiment. I: Single-layer cloud, Q. J. R. Meteorol. Soc. A J. Atmos. Sci. Appl. Meteorol. Phys. Oceanogr., 135, 979–1002, https://doi.org/10.1002/qj.416, 2009.

Knote, C., Tuccella, P., Curci, G., Emmons, L., Orlando, J. J., Madronich, S., Baró, R., Jiménez-Guerrero, P., Luecken, D., and Hogrefe, C.: Influence of the choice of gas-phase mechanism on predictions of key gaseous pollutants during the AQMEII phase-2 intercomparison, Atmos. Environ., 115, 553–568, https://doi.org/10.1016/j.atmosenv.2014.11.066, 2015.

Kong, L., Tang, X., Zhu, J., Wang, Z., Fu, J. S., Wang, X., Itahashi, S., Yamaji, K., Nagashima, T., and Lee, H.-J.: Evaluation and uncertainty investigation of the NO_2, CO and NH_3 modeling over China under the framework of MICS-Asia III, Atmos. Chem. Phys., 20, 181–202, https://doi.org/10.5194/acp-20-181-2020, 2020.

Li, J., Nagashima, T., Kong, L., Ge, B., Yamaji, K., Fu, J. S., Wang, X., Fan, Q., Itahashi, S., and Hyo-Jung, L.: Model evaluation and intercomparison of surface-level ozone and relevant species in East Asia in the context of MICS-Asia Phase III–Part 1: Overview, Atmos. Chem. Phys., 19, 12993–13015, https://doi.org/10.5194/acp-19-12993-2019, 2019.

Li, M., Liu, H., Geng, G., Hong, C., Liu, F., Song, Y., Tong, D., Zheng, B., Cui, H., and Man, H.: Anthropogenic emission inventories in China: a review, Natl. Sci. Rev., 4, 834–866, https://doi.org/10.1093/nsr/nwx150, 2017.

Liu, Z., Wang, Y., Hu, B., Lu, K., Tang, G., Ji, D., Yang, X., Gao, W., Xie, Y., and Liu, J.: Elucidating the quantitative characterization of atmospheric oxidation capacity in Beijing, China, Sci. Total Environ., 771, 145306, https://doi.org/10.1016/j.scitotenv.2021.145306, 2021.

Ma, Y., Jin, Y., Zhang, M., Gong, W., Hong, J., Jin, S., Shi, Y., Zhang, Y., and Liu, B.: Aerosol optical properties of haze episodes in eastern China based on remote-sensing observations and WRF-Chem simulations, Sci. Total Environ., 757, 143784, https://doi.org/10.1016/j.scitotenv.2020.143784, 2021.

Mailler, S., Menut, L., Khvorostyanov, D., Valari, M., Couvidat, F., Siour, G., Turquety, S., Briant, R., Tuccella, P., and Bessagnet, B.: CHIMERE-2017: from urban to hemispheric chemistry-transport modeling, Geosci. Model Dev., 10, 2397–2423, https://doi.org/10.5194/gmd-10-2397-2017, 2017.

Makar, P. A., Gong, W., Milbrandt, J., Hogrefe, C., Zhang, Y., Curci, G., Žabkar, R., Im, U., Balzarini, A., Baró, R., Bianconi, R., Cheung, P., Forkel, R., Gravel, S., Hirtl, M., Honzak, L., Hou, A., Jiménez-Guerrero, P., Langer, M., Moran, M. D., Pabla, B., Pérez, J. L., Pirovano, G., San José, R., Tuccella, P., Werhahn, J., Zhang, J., and Galmarini, S.: Feedbacks between air pollution and weather, Part 1: Effects on weather, Atmos. Environ., 115, 442–469, https://doi.org/10.1016/j.atmosenv.2014.12.003, 2015a.

Makar, P. A., Gong, W., Hogrefe, C., Zhang, Y., Curci, G., Žabkar, R., Milbrandt, J., Im, U., Balzarini, A., Baró, R., Bianconi, R., Cheung, P., Forkel, R., Gravel, S., Hirtl, M., Honzak, L., Hou, A., Jiménez-Guerrero, P., Langer, M., Moran, M. D., Pabla, B., Pérez, J. L., Pirovano, G., San José, R., Tuccella, P., Werhahn, J., Zhang, J., and Galmarini, S.: Feedbacks between air pollution and weather, part 2: Effects on chemistry, Atmos. Environ., 115, 499–526, https://doi.org/10.1016/j.atmosenv.2014.10.021, 2015b.

Menut, L., Bessagnet, B., Khvorostyanov, D., Beekmann, M., Blond, N., Colette, A., Coll, I., Curci, G., Foret, G., and Hodzic, A.: CHIMERE 2013: a model for regional atmospheric composition modelling, Geosci. Model Dev., 6, 981–1028, https://doi.org/10.5194/gmd-6-981-2013, 2013.

Qu, Y., Voulgarakis, A., Wang, T., Kasoar, M., Wells, C., Yuan, C., Varma, S., and Mansfield, L.: A study of the effect of aerosols on surface ozone through meteorology feedbacks over China, Atmos. Chem. Phys., 21, 5705–5718, https://doi.org/10.5194/acp-21-5705-2021, 2021.

Rosenfeld, D., Andreae, M. O., Asmi, A., Chin, M., de Leeuw, G., Donovan, D. P., Kahn, R., Kinne, S., Kivekäs, N., and Kulmala, M.: Global observations of aerosol-cloud-precipitation-climate interactions, Rev. Geophys., 52, 750–808, https://doi.org/10.1002/2013RG000441, 2014.

Safieddine, S., Boynard, A., Coheur, P.-F., Hurtmans, D., Pfister, G., Quennehen, B., Thomas, J. L., Raut, J.-C., Law, K. S., and Klimont, Z.: Summertime tropospheric ozone assessment over the Mediterranean region using the thermal infrared IASI/MetOp sounder and the WRF-Chem model, Atmos. Chem. Phys., 14, 10119–10131, https://doi.org/10.5194/acp-14-10119-2014, 2014.

Stein, O., Schultz, M. G., Bouarar, I., Clark, H., Huijnen, V., Gaudel, A., George, M., and Clerbaux, C.: On the wintertime low bias of Northern Hemisphere carbon monoxide found in global model simulations, Atmos. Chem. Phys., 14, 9295–9316, https://doi.org/10.5194/acp-14-9295-2014, 2014.

Tang, W., Yang, K., Qin, J., Li, X., and Niu, X.: A 16-year dataset (2000–2015) of high-resolution (3 h, 10 km) global surface solar radiation, Earth Syst. Sci. Data, 11, 1905–1915, https://doi.org/10.5194/essd-11-1905-2019, 2019.

Tuccella, P., Menut, L., Briant, R., Deroubaix, A., Khvorostyanov, D., Mailler, S., Siour, G., and Turquety, S.: Implementation of aerosol-cloud interaction within WRF-CHIMERE online coupled model: Evaluation and investigation of the indirect radiative effect from anthropogenic emission reduction on the Benelux Union, Atmosphere (Basel)., 10, https://doi.org/10.3390/atmos10010020, 2019.

Wallace, J. M. and Hobbs, P. V: Atmospheric science: an introductory survey, Elsevier, 2006.

Wang, K., Zhang, Y., Yahya, K., Wu, S.-Y., and Grell, G.: Implementation and initial application of new chemistry-aerosol options in WRF/Chem for simulating secondary organic aerosols and aerosol indirect effects for regional air quality, Atmos. Environ., 115, 716–732, https://doi.org/10.1016/j.atmosenv.2014.12.007, 2015.

Wang, K., Zhang, Y., Zhang, X., Fan, J., Leung, L. R., Zheng, B., Zhang, Q., and He, K.: Fine-scale application of WRF-CAM5 during a dust storm episode over East Asia: Sensitivity to grid resolutions and aerosol activation parameterizations, Atmos. Environ., 176, 1–20, https://doi.org/0.1016/j.atmosenv.2017.12.014, 2018.

Wang, K., Zhang, Y., Yu, S., Wong, D. C., Pleim, J., Mathur, R., Kelly, J. T., and Bell, M.: A comparative study of two-way and offline coupled WRF v3.4 and CMAQ v5.0.2 over the contiguous US: performance evaluation and impacts of chemistry–meteorology feedbacks on air quality, Geosci. Model Dev., 14, 7189–7221, https://doi.org/10.5194/gmd-14-7189-2021, 2021.

Wang, K., Gao, C., Wu, K., Liu, K., Wang, H., Dan, M., Ji, X., and Tong, Q.: ISAT v2. 0: an integrated tool for nested-domain configurations and model-ready emission inventories for WRF-AQM, Geosci. Model Dev., 16, 1961–1973, https://doi.org/10.5194/gmd-16-1961-2023, 2023.

Wang, S. and Hao, J.: Air quality management in China: Issues, challenges, and options, J. Environ. Sci., 24, 2–13, https://doi.org/10.1016/S1001-0742(11)60724-9, 2012.

Wang, Z., Wang, Z., Li, J., Zheng, H., Yan, P., and Li, J.: Development of a meteorology-chemistry two-way coupled numerical model (WRF-NAQPMS) and its application in a severe autumn haze simulation over the Beijing-Tianjin-Hebei area, China. Clim, Environ. Res, 19, 153–163, https://doi.org/10.3878/j.issn.1006-9585.2014.13231, 2014.

Wiedinmyer, C., Akagi, S. K., Yokelson, R. J., Emmons, L. K., Al-Saadi, J. A., Orlando, J. J., and Soja, A. J.: The Fire INventory from NCAR (FINN): A high resolution global model to estimate the emissions from open burning, Geosci. Model Dev., 4, 625–641, https://doi.org/10.5194/gmd-4-625-2011, 2011.

Wong, D. C., Pleim, J., Mathur, R., Binkowski, F., Otte, T., Gilliam, R., Pouliot, G., Xiu, A., Young, J. O., and Kang, D.: WRF-CMAQ two-way coupled system with aerosol feedback: software development and preliminary results, Geosci. Model Dev., 5, 299–312, https://doi.org/10.5194/gmd-5-299-2012, 2012.

Xing, J., Mathur, R., Pleim, J., Hogrefe, C., Wang, J., Gan, C.-M., Sarwar, G., Wong, D. C., and McKeen, S.: Representing the effects of stratosphere–troposphere exchange on 3-D O_3 distributions in chemistry transport models using a potential vorticity-based parameterization, Atmos. Chem. Phys., 16, 10865–10877, https://doi.org/10.5194/acp-16-10865-2016, 2016.

Xing, J., Wang, J., Mathur, R., Wang, S., Sarwar, G., Pleim, J., Hogrefe, C., Zhang, Y., Jiang, J., and Wong, D. C.: Impacts of aerosol direct effects on tropospheric ozone through changes in atmospheric dynamics and photolysis rates, Atmos. Chem. Phys., 17, 9869–9883, https://doi.org/10.5194/acp-17-9869-2017, 2017.

Xu, K.-M. and Randall, D. A.: A semiempirical cloudiness parameterization for use in climate models, J. Atmos. Sci., 53, 3084–3102, https://doi.org/10.1175/1520-0469(1996)053<3084:ASCPFU>2.0.CO;2, 1996.

Zaveri, R. A., Easter, R. C., Fast, J. D., and Peters, L. K.: Model for simulating aerosol interactions and chemistry (MOSAIC), J. Geophys. Res. Atmos., 113, https://doi.org/10.1029/2007JD008782, 2008.

Zhang, X., Wu, Y., Liu, X., Reis, S., Jin, J., Dragosits, U., Van Damme, M., Clarisse, L., Whitburn, S., and Coheur, P.-F.: Ammonia emissions may be substantially underestimated in China, Environ. Sci. Technol., 51, 12089–12096, https://doi.org/10.1021/acs.est.7b02171, 2017.

Zhang, Y.: Online-coupled meteorology and chemistry models: history, current status, and outlook, Atmos. Chem. Phys, 8, 2895–2932, https://doi.org/10.5194/acp-8-2895-2008, 2008.

Zhang, Y., Zhang, X., Wang, K., Zhang, Q., Duan, F., and He, K.: Application of WRF/Chem over East Asia: Part II. Model improvement and sensitivity simulations, Atmos. Environ., 124, 301–320, https://doi.org/10.1016/j.atmosenv.2015.07.023, 2016.

Zhao, B., Liou, K., Gu, Y., Li, Q., Jiang, J. H., Su, H., He, C., Tseng, H.-L. R., Wang, S., and Liu, R.: Enhanced PM2.5 pollution in China due to aerosol-cloud interactions, Sci. Rep., 7, 1–11, https://doi.org/10.1038/s41598-017-04096-8, 2017.

Zhou, C., Zhang, X., Gong, S., Wang, Y., and Xue, M.: Improving aerosol interaction with clouds and precipitation in a regional chemical weather modeling system, 16, 145–160, https://doi.org/10.5194/acp-16-145-2016, 2016.

Zhu, J., Wang, S., Wang, H., Jing, S., Lou, S., Saiz-Lopez, A., and Zhou, B.: Observationally constrained modeling of atmospheric oxidation capacity and photochemical reactivity in Shanghai, China, Atmos. Chem. Phys., 20, 1217–1232, https://doi.org/10.5194/acp-20-1217-2020, 2020.

Zhu, J., Chen, L., Liao, H., Yang, H., Yang, Y., and Yue, X.: Enhanced $PM_{2.5}$ decreases and O_3 increases in China during COVID-19 lockdown by aerosol-radiation feedback, Geophys. Res. Lett., 48, 1–11, https://doi.org/10.1029/2020GL090260, 2021.